Impact of southeast Indian Ocean sea surface temperature anomalies on monsoon-ENSO-dipole variability in a coupled ocean-atmosphere model

Pascal Terray, Fabrice Chauvin, Hervé Douville

Impact of southeast Indian Ocean Sea Surface Temperature anomalies on monsoon-ENSO-dipole variability in a coupled ocean-atmosphere model

by

Pascal Terray[1], Fabrice Chauvin[2] and Hervé Douville[2]

[1] LOCEAN, Institut Pierre Simon Laplace (IPSL) and Université Paris 7, Paris, France

[2] Météo-France CNRM/GMGEC/UDC, Toulouse, France

Submitted to Climate Dynamics *January, 2006*

Accepted *August 2006*

Corresponding author address: Pascal Terray, LOCEAN/IPSL, Université Pierre et Marie Curie, BP 100, 4 Place Jussieu, 75252 Paris CEDEX 05, France.
E-mail: terray@lodyc.jussieu.fr

Abstract

Recent studies show that SouthEast Indian Ocean (SEIO) SSTs are a highly significant precursor of transitions of the whole monsoon-El Niño-Southern Oscillation (ENSO) system during recent decades. However, the reasons for this specific interannual variability have not yet been identified unequivocally from the observations.

Among these, the possibility of SEIO SST-driven variability in the monsoon-ENSO system is investigated here by inserting positive/negative SEIO temperature anomalies in the February's restart files of a state-of-the-art coupled General Circulation Model (GCM) for 49 years of a control simulation. For each year of the control simulation, the model was then integrated for a one year period in fully coupled mode. These experiments show that Indian Summer Monsoon (ISM) and tropical Indian Ocean Dipole Mode (IODM) events are significantly influenced by the SEIO temperature perturbations inserted in the mixed layer of the coupled GCM several months before. A warm SEIO perturbation, inserted in late boreal winter, slowly propagates northward during the following seasons, implies enhanced ISM rainfall and finally triggers a negative IODM pattern during boreal fall in agreement with observations. A reversed evolution is simulated for a cold SEIO perturbation. It is shown that the life cycle of the simulated SEIO signal is driven by the positive wind-evaporation-SST, coastal upwelling and wind-thermocline-SST feedbacks. Further diagnosis of the sensitivity experiments suggests that stronger ISM and IODM variabilities are generated by excluding the El Niño years of the control simulation or when the initial background state in the SEIO is warmer. This finding confirms that IODM events may be triggered by multiple factors, other than ENSO, including subtropical SEIO SST anomalies.

However, the ENSO mode does not react significantly to the SEIO temperature perturbation in the perturbed runs even though the simulated Pacific pattern agrees with the observations during boreal fall. These discrepancies with the observations may be linked to model biases in the Pacific and to the too strong ENSO simulated by this coupled GCM.

These modeling evidences confirm that subtropical Indian Ocean SST anomalies generated by Mascarene high pulses during austral summer are a significant precursor of both ISM and IODM events occuring several months later.

1. Introduction

There is now abundant evidence that Indian Ocean Sea Surface Temperature (SST) plays an important role in tropical climate variability. SSTs and coupled ocean-atmosphere interactions in the Indian Ocean are now recognized as a significant factor in El Niño-Southern Oscillation (ENSO) evolution (Kim and Lau, 2001; Yu et al., 2003; Meehl et al., 2003; Behera and Yamagata, 2003; Wu and Kirtman, 2004b; Terray and Dominiak, 2005; Kug et al., 2005; Annamalai et al., 2005a). Wu and Kirtman (2004b) found that Indian Ocean SST anomalies affect ENSO through the modulation of the Pacific and Indian oceans Walker circulation in their coupled simulations. Some evidences were also presented for the role of Indian Ocean in linking ENSO to the Asian Summer Monsoon (Meehl and Arblaster, 2002ab; Terray et al., 2003; Wang et al., 2003; Wu and Kirtman, 2004a). Wang et al. (2003) suggested that an anomalous SouthEast Indian Ocean (SEIO) anticyclone sustained by local air-sea interactions plays a fundamental role in the evolution of the Asian-Australian monsoon system during boreal summer and fall of developing El Niño years. Wu and Kirtman (2004a) examined the impacts of the Indian Ocean on the ENSO-Indian Summer Monsoon (ISM) relationship with a coupled atmosphere-ocean General Circulation Model (GCM). Their results showed that the ISM-ENSO relationship reverses sign when the Indian Ocean is decoupled from the atmosphere. Furthermore, several studies have demonstrated that Indian Ocean SST anomalies enhance the anomalous anticyclone which is established over the western North Pacific in the mature phase of El Niño (Watanabe and Jin, 2002; Annamalai et al., 2005b). This low-level anomalous anticyclone plays an important role in the relationship between ENSO and the east Asian climate (Wang and Zhang, 2002; Wang et al. 2003). Finally, it has even been suggested that the origin of the Tropospheric Biennial Oscillation (TBO) may arise from coupled processes within the tropical Indian Ocean (Chang and Li, 2000; Li et al., 2001; Meehl and Arblaster, 2002b). All these findings confirm the importance of air-sea interactions in the Indian Ocean for the proper simulation of the whole monsoon-ENSO system (Kumar et al., 2005; Wang et al., 2005). However, despite these recent advances, some scientifically challenging questions remain to be solved about the role of Indian Ocean SSTs at interannual time scales. We review some of these issues in the rest of this introduction.

Recent studies also suggest the existence of coupled dynamics in the Indian Ocean which give rise to strong interannual climate anomalies in the Indian areas. The SST Indian Ocean Dipole

Mode (IODM), which peaks during boreal fall and is linked to rainfall anomalies in East Africa is one of such phenomena (Saji et al., 1999; Webster et al., 1999; Behera et al., 2005, 2006). Another SST dipole mode in the southern Indian Ocean, seasonally phase-locked to the austral summer, has also been documented by Behera and Yamagata (2001). Such subtropical events are associated to Mascarene high pulses during austral summer and are found to produce significant climate anomalies in southern Africa during boreal spring (Goddard and Graham, 1999; Reason, 2002). However, the links between these spring/fall Indian Ocean dipole events and the monsoon-ENSO system are still a controversial issue (Allan et al., 2001; Yamagata et al., 2002). A recurrent question is how much of IODM variability is forced by ENSO or triggered by local air-sea interactions or other factors (Gualdi et al., 2003; Lau and Nath, 2004; Shinoda et al., 2004; Fischer et al., 2005; Behera et al., 2006). Although there is a whole body of literature about this phenomenon, the mechanisms that excite coupled air-sea interactions in the eastern Indian Ocean during boreal fall are not yet identified unequivocally (Gualdi et al., 2003□Spencer et al, 2005; Fischer et al., 2005; Behera et al., 2006). Another question of contention is the relationship between IODM events and ISM variability. One suggestion is that positive IODM events enhance ISM rainfall (Ashok et al. 2001; Li et al. 2003; Ashok et al. 2004), although Li et al. (2003) propose that the strong ISM will damp the original IODM event. Furthermore, Ashok et al. (2001, 2004) argue that influence of IODM on ISM is opposite to the effect of ENSO. Others suggest that positive IODM events normally coincide with dry conditions over the Indian subcontinent and that IODM is an integral part of the coupled TBO system (Webster et al., 2002; Loschnigg et al., 2003, Meehl et al. 2003). Furthermore, the correct simulation of the reciprocal influence between ISM variability and tropical Indian Ocean SST anomalies remains a challenge for state-of-the-art coupled models (Cherchi et al., 2006). Thus, a better understanding of the linkages of ISM rainfall and circulation anomalies with IODM events will be also a welcome contribution to the literature.

Another intriguing problem is the exact role of southern Indian Ocean SSTs and how they contribute to the transitions of the whole monsoon-ENSO-IODM system. Nicholls (1995) and Terray et al. (2003) found that warm (cold) SEIO SST anomalies during boreal winter are significantly related to strong (weak) ISMs several months later. Terray et al. (2005b) suggest that SEIO SSTs induced by Mascarene high pulses during late boreal winter is the unique common SST precursor of ISM, ENSO and IODM events after the 1976-77 regime shift. Additionally, these subtropical SST anomalies may be a trigger for the anomalous low-level

SEIO anticyclone documented by Wang et al. (2003) through both the wind-evaporation-SST and wind-thermocline-SST positive feedbacks (Terray et al., 2005b). Furthermore, Terray and Dominiak (2005) suggest that SEIO SST anomalies produce a persistent forcing on ENSO by inducing local wind anomalies over the Pacific warm pool and modulating the regional Hadley cell in the southwest Pacific after the 1976-1977 regime shift. These findings may explain why SEIO SSTs is among the best predictors if we attempt to predict ENSO across the spring persistence barrier during recent decades (Kug et al., 2005; Dominiak and Terray, 2005). However, rigorously speaking, these observational results show nothing more than concurrent variations in different quantities and do not allow the identification and contribution of the different mechanisms involved. The mechanisms by which SEIO SST anomalies exert a forcing on the evolution of the whole monsoon-ENSO-IODM system still remain to be investigated through careful numerical coupled ocean-atmosphere experiments.

The primary goal of this study is to further investigate the spatiotemporal characteristics of Indian Ocean SSTs and their relationships with ISM, as well as other modes of variability such as IODM or ENSO by using a state-of-the-art coupled GCM. A series of numerical experiments, using a fully coupled GCM, with idealized initial conditions (e.g. a prescribed SEIO temperature anomaly during late boreal winter) have been carried out for elucidating the physical processes responsible for the statistical associations between SEIO SST anomalies and the monsoon-ENSO-IODM system. A brief review of the coupled model is given in section 2, along with a description of our sensitivity numerical tests and observed datasets that are used to validate the model control simulation. The annual cycle and interannual variability of the Indo-Pacific climate as reproduced in the control experiment are first analyzed in section 3. The hypothesis that SEIO SST anomalies play a significant role in the coupled climate system has then been tested in suitably chosen coupled numerical experiments by inserting temperature anomalies in the SEIO during February in the coupled model. This series of numerical experiments is reported in section 4. This is followed by discussion and conclusions in section 5.

2. Model, experiment design and observed datasets

a. The coupled model

Since our primary goal relates to ISM interannual variability, we selected a coupled GCM

whose precipitation climatology during boreal summer over the Indian Ocean is reasonably close to the observed climatology (see Fig. 3). The selected GCM is the Centre National de Recherches Météorologiques coupled climate model, CNRM-CM2. This coupled GCM has been used for both seasonal forecasting (Guérémy et al. 2005) and climate change (Douville et al. 2002, Ashrit et al. 2003, Douville 2005) experiments.

This coupled model includes the ARPEGE-Climat atmospheric GCM version 3 (Déqué et al., 1994), the OPA oceanic GCM (Madec et al., 1998), the GELATO sea ice model (Salas Mélia, 2002) and the ISBA land surface model (Noilhan and Mahfouf, 1996). The atmospheric GCM gives fluxes of heat, freshwater and momemtum to the oceanic GCM, and the oceanic GCM gives the SST to the atmospheric GCM through the OASIS coupler on a daily time step without any flux adjustment (Valcke et al., 2000). The atmospheric model has a T63 spectral truncation and a linear Gaussian grid with a quasi uniform spacing of about 2° in latitude and longitude. The vertical resolution consists of 45 vertical levels. The ocean model (OPA, see Madec et al., 1997) is a finite difference model with an horizontal grid with a variable horizontal resolution (2° in longitude and a latitude interval of 0.5° at the equator which increases poleward). It has 31 vertical levels with a much higher vertical resolution in the boundary layer (10m) than in the deep ocean (500m). Note that both Sumatra and Java islands are represented in the OPA model. This is particularly important for a fair representation of IODM variability in the coupled GCM (Spencer et al., 2005).

In this study, we first use a «□ontrol□ simulation spanning 49 years. In this control experiment, the coupled GCM is integrated without any flux adjustment and initialized with oceanic temperature and salinity profiles from Levitus (1982), and with atmospheric trace gas concentrations observed in the 1950's. The greenhouse gases and sulfate aerosols concentrations are then updated each year according to observations from 1950 to 1998. The basic state and interannual variability of the Indo-Pacific climate as simulated in this control run is described in section 3. Standard regression and correlation techniques have been used for this purpose. The statistical significance of the correlation/regression coefficients have been assessed with a phase-scrambling bootstrap test (Davison and Hinkley, 1997). No filtering is applied to the various simulated fields before statistical analysis.

b. Design of the sensitivity experiments

To address if and how the SEIO SSTs can affect the ISM-ENSO-IODM system, we have

performed ensembles of short integrations starting from different (atmospheric and oceanic) February's initial conditions derived from the control simulation of the CNRM coupled model, but with the same SEIO temperature perturbation inserted in these initial conditions.

More precisely, the coupled GCM is periodically restarted during the control integration and SST, sea ice distribution, as well as atmospheric and land surface conditions are saved. In particular, the coupled GCM has been restarted in February of each year, though the exact date of the restarts varies from year to year in the control integration. To test our hypothesis about the role of boreal winter SEIO SST anomalies, we performed ensembles of short integrations where we have added a temperature anomaly of +/-1°K on the first two levels and of +/- 0.5°K on the third level of the OPA model in the SEIO (71-121°E, 10°-30°S), with a weight of 0.5 on the limits of the domain, in the February restarts of the coupled GCM. The number of layers for prescribing temperature anomalies was estimated according to the February mean depth of the mixed layer (25 m) in the SEIO in the control simulation (Fig. 1). The geographical domain for this idealized temperature perturbation (indicated by a black frame in Fig. 1) has been determined from the observational study of Terray et al. (2005b) who have derived their composite analyses from a February-March SEIO SST index computed in the domain 72°-122°E and 4°-26°S. However, the SEIO domain used here has been translated 6° to the south due to the large gradient in the mixed layer depth which is observed near 5° south in the control simulation during February (Fig. 1). Moreover, this translation of the SEIO box 6° to the south allows us to better capture the SST signal associated with subtropical dipole events in the southern Indian Ocean (Terray and Dominiak, 2005) and to clearly distinguish this SST signal from the IODM signature (recall that the eastern box which is used in the IODM index of Saji et al. (1999) is 90°-110°E, 10°S-0°). Keeping in mind the rather low SST variability observed in the SEIO (see Figs. 4a, b and also Xie et al., 2002□Fischer et al., 2005), we have chosen to prescribe only moderate values of temperature anomalies.

A positive SEIO temperature perturbation has been inserted in the February restarts of the coupled GCM for each year of the control experiment (1950-1998). For every year, the coupled model was then integrated for a 1-yr period. In other words, these short integrations differ only by their initial conditions. A series of identical experiments is also performed with a negative SEIO temperature anomaly with the same magnitude to further confirm the results. The differences between the warm and cold SEIO SST perturbed simulations are then

averaged for all years of the control simulation (e.g. 49-yr averages). In this manner, the evolution of atmospheric and oceanic anomalies associated with a positive SEIO perturbation during late boreal winter is examined. For a cold SEIO SST perturbation, the anomalies reverse sign. To examine the sensitivity of the effect of SEIO temperature perturbations to the initial background state or model errors, the composite differences have also been recomputed from different subsets of years in the control simulation. These additional sensitivity experiments are further described in section 4.

A local statistical test is applied to the various composite differences in order to assess the statistical significance of the results. More precisely, the statistical significance of the differences was estimated through the procedure in Noreen (1989), based on a permutation test with 9999 shuffles, and differences significant at the 90% confidence level have been shaded in the figures. More details about this statistical test are given in Terray et al. (2003).

c. observed datasets

The NCEP/NCAR reanalysis (Kalnay et al., 1996), the version2 of the Extended Reconstruction of global SST (ERSST) developed by Smith and Reynolds (2004) and the CRU TS 2.0 rainfall dataset (Mitchell et al., 2003) have been used to validate the control simulation from the CNRM coupled model. All the observations and reanalysis datasets are taken from the period 1950-1998 to be consistent with the model control simulation.

3. The coupled GCM basic state and interannual variability

The model performance has been examined in previous studies and is only briefly summarized here (Ashrit et al., 2003; Camberlin et al., 2004). We will mainly focus on salient features of the simulated Indo-tropical climate that will be relevant to interpret the results of the numerical experiments reported in the next section.

The bimonthly mean climatologies of rainfall, 850 hPa wind and SST computed from the 49 years of the control simulation in the Indo-Pacific areas are presented in Figure 2. The CNRM coupled model qualitatively represents many aspects of the observed precipitation, SST and low-level wind mean fields over the Indo-Pacific areas (not shown). However, stronger easterly trade winds are simulated in the tropical Pacific associated with the formation of an

unrealistic double Inter Tropical Convergence Zone (ITCZ) structure year around (Figs 2a-f). These systematic errors are typical of many coupled models without flux adjustment (AchutaRao and Sperber, 2002; Guilyardi et al., 2003; Turner et al., 2005). Figure 3 shows the observed and simulated mean annual cycle of rainfall over India (spatial average over land grid points between 5-30°N and 70-95°E; IMR hereafter) and of the Indian Monsoon Dynamical Index (IMDI) proposed by Wang et al. (2001). The IMDI is computed as the difference in 850 hPa zonal winds averaged over 5-15°N/40-80°E and 20-30°N/70-90°E, respectively, and represents the dominant mode of interannual variability in the Indian areas during boreal summer (Wang et al., 2001). A particular strength for our numerical experiments is that this version of the CNRM coupled model performs a realistic simulation of the IMR annual cycle with a strong increase in precipitation over the Indian subcontinent during boreal summer associated with the reversal of the low-level winds over the North Indian Ocean (Fig. 3). The simulated annual cycle of IMDI is also in relatively good agreement with the observations in all months even if the amplitude of this simulated annual cycle is slightly stronger than observed (Fig. 3b). In other words, the CNRM coupled model captures reasonably well the amplitude of the Indian monsoon annual cycle. Over the tropical Indian Ocean, abundant rainfall is simulated too westward from boreal spring to fall. However, the reversal of the winds along the shores of Java and Sumatra is reasonably well captured (Figs. 2a-f). This is particularly important for a good representation of the coastal upwelling feedback which was thought to be important for the evolution of SST SEIO anomalies (Terray et al., 2005b). Overall, simulated SSTs are characterized by a general warm bias in the tropics with the main discrepancies found at eastern boundary oceanic current areas near subtropical latitudes (Camberlin et al., 2004). Superimposed onto this global warm error, there is a cold tongue bias in the central and eastern equatorial Pacific associated with the double ITCZ structure and the westward extension of the easterly trade winds (Figs. 2g-l). These features suggest an overactive upwelling of cold water in the central equatorial Pacific associated with the stronger easterly winds via Ekman divergence.

The bimonthly standard-deviations of the observed and simulated SST fields are shown in Figure 4. The simulated equatorial Pacific variability extends too far west and is exagerated compared to the observations. The standard-deviation of the Niño-3.4 (5°S-5°N, 170-120°W) SST anomalies during boreal winter stands at 2°C as compared to 1.1°C for observed data. This is in contrast with most other coupled models without flux adjustement which exhibit

reduced Niño-3.4 SST interannual variability (AchutaRao and Sperber, 2002; Terray et al., 2005a). This exagerated ENSO mode is likely to lead to model errors in the Indian Ocean and to stronger than observed teleconnection patterns (Camberlin et al., 2004). However, the simulated SST variability associated with ISM and IODM is correctly locked along the east coast of Africa and to the south of Sumatra, respectively (Figs 4d-f and 4j-l). The local variability maximum located off Sumatra is stronger than observed during boreal fall (1.2°C as compared to 0.4-0.6°C for observed data). This suggests that the wind-SST-thermocline feedback is too active in the eastern Indian Ocean (Fischer et al., 2005). The local variability maxima simulated in the South central Indian Ocean and off the west coast of Australia during boreal winter are also too intense. All these discrepancies are related to the exagerated ENSO teleconnection patterns as we will see below. However, it is noteworthy that both IODM and ENSO SST variabilities are correctly phase-locked to the annual cycle with maxima of SST standard-deviations observed during boreal fall and winter, respectively (Figs 4k, l).

Figure 5 shows the seasonal evolution of simulated correlations between the December-January mean Niño-3.4 SST time series and SSTs in the Indian and Pacific oceans. The correlations are calculated beginning one year prior to the Niño3.4 SST. Similar analyses have been conducted from the observations for periods before and after the so called 1976-77 climate shift by Wang (1995) and Terray and Dominiak (2005). A clear ENSO signal is depicted with a westward propagation of warm anomalies from the eastern equatorial Pacific to the central and west Pacific during the developing ENSO year. However, the tongue of positive correlations is too meridionally confined and extends too far west. The negative correlations forming the two branches of the traditional horseshoe pattern are also splitted and much less intense than in the observations (see Terray and Dominiak, 2005; their figure 2). These biases are also shared by many coupled GCMs (AchutaRao and Sperber, 2002). This westward propagating SST signal is characteristic of the observed ENSO evolution before the 1976-77 climate shift (Wang, 1995; Wang and An, 2001; Terray and Dominak, 2005; Guilyardi, 2006). During recent decades, an eastward propagation of SST anomalies is observed. As in the period after the regime shift, the El Niño onset is preceded by a basinwide Indian Ocean cooling in the simulation (Figs. 5a, b). However, these strong negative correlations with Indian Ocean SSTs in the preceding winter may be due to the too regular and short ENSO in the model (e.g. 3-yr periodicity, see Ashrit et al. 2003). The primary

symptom of the too regular ENSO mode is the complete reversal of the correlation pattern one year apart in Figure 5. This short period (3-yr) ENSO in the control simulation could be related to the meridional confinement of the wind stress anomaly along the equatorial Pacific (See Fig. 6 and also Kirtman, 1997). This regularity of simulated ENSO mode was also noted in other coupled GCMs (Turner et al., 2005). By contrast, this precursory Indian Ocean SST signal is significantly influenced by midlatitude-tropical interactions in the observations (e.g. Mascarene High pulses, see Terray and Dominiak, 2005). Another striking similarity with the observations (after the 1976-77 climate shift) is the emergence of an SST IODM pattern by October-November of the El Niño developing year. Finally, the model reproduces the basinwide warming of the tropical Indian Ocean which is observed when El Niño is mature, but this warming is too intense (Fig. 5f). This too intense warming of the Indian Ocean is related to the overly-strong ENSO teleconnection already mentioned. Other interesting features are the tongue of negative correlations which extends from the west coast of Australia and the large positive correlations farther to the west during the maturing winter of El Niño (Fig. 5f). This pattern is in agreement with the observations (see Terray et Dominak, 2005, their figure 2), but the amplitude of the simulated correlations is also much too strong, suggesting again an enhanced remote response to ENSO in the southern Indian Ocean.

Fgure 6 shows regression coefficients of 2-month average rainfall and 850 hPa wind fields versus the December-January mean Niño-3.4 SST time series. The cold Indian Ocean SST anomalies preceding the El Niño onset are associated with a pair of low-level cyclonic anomalies straddling the equator in the eastern Indian and western Pacific oceans during February-March (Fig. 6a). These features can be attributed to Rossby wave responses to increased diabatic heating over the equatorial western Pacific associated with a maturing La Niña state which is discernible in the equatorial Pacific (Fig. 6a, see Lau and Nath, 2000, 2003). The cold eastern and central Pacific SST anomalies strengthen the Pacific Walker circulation and induce anomalous ascendance over the western equatorial Pacific and maritime continent (Figs. 5a and 6a). The anomalous western north Pacific cyclone merges with a large anticlockwise circulation anomaly located over the North Pacific in the simulation (Figs 6a, b). This last center is part of the pronounced wave train pattern emanating from the central Pacific, crossing the north Pacific and extending to north America during the maturing winter of La Niña. It is well-known that this Pacific-North American teleconnection pattern is excited by ENSO during boreal winter (Wallace and Gutzler, 1981). However, this

pattern does not show up before ENSO transitions in the observations (Wang, 1995; Terray et al., 2005b; Terray and Dominiak, 2005). These circulation errors are consistent with the regularity of the simulated ENSO mode, but lead to improper representation of the pre-El Niño atmospheric patterns.

The anomalous low-level cyclone which is established over the western North Pacific during the maturing winter of La Niña persists through the following spring while the corresponding cyclone over the southeast Indian Ocean quickly fades away and is replaced by a weak anticyclonic circulation (Figs. 6b, c). Figures 5 and 6 suggest that Indian Ocean SST anomalies play a role in the persistence of this anomalous low-level cyclone over the western North Pacific through its modulation of the Walker circulation. (Watanabe and Jin, 2002, Annamalai et al., 2005b). This is further supported by the fact that Pacific SST anomalies diminish one season earlier than the anomalous cyclone while the basinwide Indian Ocean cooling persists through the following spring and early summer (Figs. 5b, c). This Indian Ocean cooling which occurs in response to La Niña may then partly force the transition from La Niña to El Niño (and vice-versa) in the control simulation (Meehl and Arblaster, 2002ab; Meehl et al., 2003). When the Indian Ocean is cold, the persistent westerly wind anomalies associated with the western North Pacific cyclone can induce eastward advection of warm water and eastward-propagating downwelling Kelvin waves which will deepen the thermocline to the east. These waves may subsequently trigger the reversal of SST anomalies off the South America coast and favor an El Niño event. In contrast, when the Indian Ocean is warm, the induced easterlies over the western equatorial Pacific can shoal the thermocline in the eastern equatorial Pacific and enhance the ongoing La Niña event (reversed patterns in Figures 5 and 6).

However, this mechanism by which Indian Ocean SST anomalies that develop during the mature phase of El Niño (La Niña) may negatively feedback on the ENSO mode is fundamentally different from the scenario proposed in Terray et al. (2005b). In the observations, southern Indian Ocean SST anomalies, produced by Mascarene high pulses during boreal winter, trigger coupled air-sea processes in the eastern Indian Ocean during the following boreal spring, summer and fall. This induces a remote forcing on the whole monsoon-ENSO-IODM system after the 1976-77 regime shift (Terray and Dominiak, 2005). Apparently, this coupled GCM is not able to reproduce these coupled interactions and different mechanisms govern the relationship between Indian Ocean SST and ENSO transitions in the control simulation.

This coupled model simulates correctly the well-documented inverse relationship between ISM and El Niño (Webster et al., 1998). Weak (strong) ISMs typically occur during the developing year of El Niño (La Niña). Interestingly, the ENSO-induced ISM rainfall anomalies extend and gain significance during the late ISM (e.g. August-September) while ENSO influence during the early ISM (e.g. June-July) is relatively weak over the Indian subcontinent as observed (Figs 6c, d□see Terray et al., 2003). Dry conditions are associated with the rapid growth of low-level anticyclonic anomalies on both sides of the equator over the eastern Indian Ocean from June-July to August-September. Furthermore, these anomalous anticyclones are located to the northwest and southwest of a significant rainfall anomaly over the maritime continent and the far eastern Indian Ocean during the whole boreal summer. This suggests that the ENSO-related ISM rainfall anomalies developed as a Matsuno-Gill type response to suppressed convective heating over the Maritime continent which is induced by the eastward displacement of the ascending branch of the Pacific Walker circulation during El Niño years in the control simulation (Gill, 1980). These details of the ISM-ENSO relationship compare well with observational and other modeling results (e.g. Lau and Nath, 2000, 2003). However, overall strong rainfall and atmospheric responses over the Indian Ocean arise from the stronger simulated ENSO mode during the maturing phase of El Niño (Figs. 6e, f). Finally, It is worth mentioning that this coupled model captures the ISM-SEIO SST relationship as documented in Terray et al. (2003). Late boreal winter SEIO SSTs induce a contrasted ISM response in the control simulation, with a weaker monsoon circulation over the north Arabian Sea during the early ISM, but a stronger monsoon circulation and enhanced rainfall over India during the late ISM (not shown).

In summary, the model captures some aspects of the ISM-ENSO-IODM system despite of the stronger simulated ENSO mode.

4. Sensitivity experiments

Due to the stronger simulated ENSO in the control simulation, the possibility of a SEIO SST-driven mode of variability is investigated here in ensembles of short coupled GCM integrations where we specify temperature anomalies in the SEIO during late boreal winter (February) and see if the ISM-ENSO-IODM system responds in the way described in the

previous observational studies (Terray et al., 2003, 2005b). The composite differences between the warm and cold SEIO perturbations experiments are attributed to the effects of the initial SEIO temperature perturbation. We first examined the composite differences formed by averaging all the warm minus cold SEIO temperature integrations (see section 2).

a. All years composites

Since the tropospheric circulation would hardly change significantly if there were no persistence of the temperature anomaly inserted in the coupled GCM, we first investigate this aspect of the numerical experiments by computing differences between simulated SST fields of the warm and cold SEIO experiments averaged over all the years from March-April before ISM to January-February after ISM (Fig. 7). The amplitude of SEIO SST differences between the cold and warm SEIO experiments shows a decay and looses significance during boreal spring and early boreal summer (Figs. 7a, b). However, these SST anomalies tend to persist and slowly move northward. The positive SST anomalies reach the coast of Java, subsequently reinvigorate and gain significance during July-August (Fig. 7c). These SST anomalies further propagate northward and are locked to the coast of Sumatra during September-November (Fig. 7d). Interestingly, the stronger positive SST signal is now found in the region that is used to define the eastern lobe of the IODM index (Saji et al., 1999). There is also a westward propagation of the positive SST signal along the equator and a negative SST perturbation in the west (south of the equator), suggesting the existence of an IODM SST pattern during fall (Figs. 7d, e). It is noteworthy that the positive SST perturbation remains highly significant at this stage, several months after the beginning of the integration. Furthermore, a consistent La Niña SST pattern emerges in the Pacific with cold SST differences in the central and eastern equatorial Pacific and a horseshoe pattern of warm SST anomalies around this region during boreal fall. However, most local differences are not significant at the 90% confidence level in the Pacific, excepted at subtropical latitudes. Finally, the positive SST perturbation in the SEIO moves southward and decays to insignificant values in January-February (Figs. 7e, f). In summary, the life cycle of the SEIO temperature perturbation is nearly one year. This composite evolution of SEIO temperature perturbations inserted in the coupled GCM is consistent with the SEIO SST composites presented in Terray et al. (2005b). This confirms the importance of SEIO SST anomalies for the transitions of the ISM-IODM-ENSO system despite the weak Pacific signal simulated

here. Due to the weak perturbation simulated in the Pacific, we concentrate on the Indian Ocean interactions in the rest of this section.

To illustrate the atmospheric response to an SEIO temperature perturbation, bimonthly 850 hPa wind and rainfall differences are presented in Figure 8.

i) March-April

During March-April, there are enhanced rainfall and large low-level cyclonic wind anomalies collocated with the positive SST perturbation in the SEIO (Fig. 8a). The SST gradients induced by the SEIO temperature perturbation force the low-level flow to converge towards the region of positive SST perturbation as expected (Lindzen and Nigam, 1987). Thus, moisture convergence increases convection and precipitation in the SEIO. On the other hand, precipitation is largely reduced near the equator and to the west of the SST perturbation, leading to a significant modulation of the ITCZ location in the southern Indian Ocean during boreal spring (Fig. 8a). Now, there are a number of processes by which this atmospheric response to the SEIO perturbation could feed back positively, maintaining the SST signal across the seasons. Two key processes are the transition of the low-level winds from westerly to easterly during spring and the wind-evaporation-SST feedback (Nicholls, 1979; Li et al., 2003; Hendon, 2003; Terray et al., 2005b). The evaporation differences between the cold and warm SEIO experiments are shown in Figure 9. Consistent with the existence of a positive wind-evaporation-SST feedback, the westerly wind anomalies between 20 and 10°S lead to reduced evaporation since the climatological winds are southeasterly over this area during March-April (Fig. 2b). This leads to surface warming through reduced latent heat fluxes associated with the decrease of the total wind speed (Fig. 9a). In contrast, over regions between the equator and 10°S with mean westerly winds during boreal spring, the generated westerly wind anomalies increase the total wind speed. The induced enhancement of evaporation and ocean mixing will cool the sea surface to the north of the SST perturbation (Fig. 7a). This may again increase the SST gradients and strengthen the SST-induced atmospheric convergence over the warm SST perturbation to the south (and to the east). Interestingly, sensible heat fluxes do not contribute significantly to the heat budget of the sea surface during spring (not shown). By contrast, surface short wave radiation provides a strong negative feedback on SST anomalies at this stage, warming the surface between the equator

and 10°S and cooling it farther south due to the increased cloudiness over the convection region (not shown). These facts confirm again the role of the wind-evaporation-SST interaction as the dominant process by which the atmosphere positively feeds back onto the ocean during boreal spring in our coupled experiments. However, the negative feedback provided by the shortwave radiation largely damps these SST fluctuations over the southern Indian Ocean during boreal spring. This may explain why the SST differences loose significance from March-April to May-June (Figs. 7a, b).

The combined interaction of the positive wind-evaporation-SST feedback with the seasonal migration of the monsoon winds will also facilitate the northward propagation of the coupled perturbation from late boreal winter to boreal summer (Figs. 8a-c). After the reversal of the monsoon wind, the cyclonic wind anomalies due to a warm SEIO SST perturbation, will decrease the total wind speed to the north of the SEIO. Consequently, these generated westerly anomalies will reduce local evaporation (Fig. 9b). This will warm the sea surface northward of the initial warm SST perturbation through latent heat fluxes (after the onset of the easterly monsoon wind) in addition to the increased shortwave radiation (Figs. 7a-c). These processes modify the SST gradients which will influence, in turn, the anomalous winds and enhance the atmospheric convergence northward of the initial SEIO SST perturbation. Due to the northward migration of the climatological monsoon winds over the south Indian Ocean from early boreal spring to boreal summer (both in the coupled GCM and real climate), this air-sea interaction favours the northward propagation of the positive SST and rainfall perturbations. A similar mechanism may be put forth to explain the propagation of a cold SEIO SST perturbation.

ii) May-June

During May-June, the positive rainfall and cyclonic circulation anomalies associated with the SST perturbation are organized in two prefered locations (Fig. 8b). One center is found in the southwest Indian Ocean, suggesting a weakening of the Mascarene high during the early ISM, and the other between Australia and Java with more intense positive rainfall anomalies. Over this area, the rainfall anomalies are also collocated with northwesterly wind anomalies locked to the west coast of Java, but these wind anomalies are just below the 90% confidence level and are masked in Figure 8b. Consistent with the two simulated cyclonic circulations, the

evaporation differences field has two minima (e.g. latent warming) in the southern tropical Indian Ocean, a broad minimum in the southwest near 65°E and 15°S and a more localized, though still significant, minimum between Australia and Java (Fig. 9b).

The May-June wind and rainfall difference fields suggest that ISM dynamics are significantly influenced by the weakening of the Mascarene high in the southwest Indian Ocean (Fig. 8b). The main perturbation appears to be a reduced interhemispheric monsoon flow with northerly wind anomalies along the Somali coast and easterly wind anomalies to the north of the equator. Consistent with these features, there is less evaporation over the Arabian Sea and decreased rainfall over the west coast of India and adjoining ocean areas (Fig. 9b). These features suggest a delayed ISM onset associated with the SEIO SST perturbation.

iii) July-August

During July-August, the difference fields first reveal a large enhancement of precipitation over the positive SST anomaly along the coast of Java while the anomalous cyclonic circulation and the positive SST differences to the west have disappeared (Figs 7c and 8c). One can also discern increased precipitation over India, the adjoining Arabian Sea and Bay of Bengal of about 1 mm day^{-1}. A large and highly significant clockwise surface circulation is associated with the enhanced precipitation off Java (Fig. 8c). Furthermore, this cyclonic atmospheric perturbation induces significant evaporation anomalies over the South Indian Ocean (Fig. 9c). By contrast, the magnitude of the SST-induced atmospheric perturbation remains small in the North Indian Ocean (Fig. 8c). The weak and insignificant evaporation anomalies to the north of the equator confirm that the enhanced ISM rainfall cannot be attributed to a strengthening of the monsoon circulation over the north Indian Ocean.

Looking back at the south Indian Ocean, there are positive evaporation differences over the central Indian Ocean and negative anomalies off the coast of Sumatra associated with the cyclonic circulation over the SEIO (Fig. 9c). First focusing to what happens in the central Indian Ocean, we observe that the significant southeasterly wind anomalies associated with the anomalous convection over the SEIO represent a strengthening of the southeast trade winds relative to climatology during boreal summer (Figs. 2d and 8c). Thus, these wind anomalies significantly reinforce the local evaporation (Fig. 9c). This also implies a cooling of the local SST through increased upper ocean mixing and latent heat fluxes as observed (Fig. 7c). Furthermore, this anomalous wind field also suggests a possible source of the

enhanced ISM precipitation during July-August (Fig. 8c). More precisely, the stronger southeast trade winds and the induced increase of the latent heat fluxes in the southern hemisphere imply an enhanced atmospheric moisture transport to the north. Once advected into the climatological westerly flow over south Asia, this anomalous moisture can increase ISM precipitation. Thus, the anomalous southeasterly flow which is the west branch of the anomalous cyclonic circulation in the SEIO establishes an interesting pathway for the southern hemisphere circulation to influence the ISM rainfall variability. This leads to the conclusion that the ISM rainfall response cannot be inferred directly from the circulation change over the North Indian Ocean and that fluctuations in atmospheric moisture transport due to circulation anomalies in the southern hemisphere play a key role in the model response. On the other hand, the prominent and significant northwesterly wind anomalies along the west coast of Java (associated with the enhanced rainfall in the SEIO) are aligned with the mean southeasterly wind observed in this area during July-August (Fig. 8c). Consequently, these northwesterly wind anomalies may reduce coastal upwelling of cooler and deeper water along the coast of Java. This coastal upwelling feedback could explain why both the SST and atmospheric anomalies reinvigorate and gain large significance once the coupled ocean-atmosphere perturbation reaches the coast of Java during summer. The importance of this process for the persistence of the warm SST perturbation is indirectly confirmed by the positive evaporation anomalies (e.g. latent cooling) locked to the coast of Java during July-August (Fig. 9c). The key-role of the coastal upwelling feedback for the growth of IODM events was also pointed out in several studies (Saji et al., 1999; Murtugudde et al., 2000). In other words, there is a clear suggestion that the positive wind-evaporation-SST feedback, which is at work during spring, may subsequently trigger a positive coastal upwelling feedback when southeasterly climatological winds reach the coast of Java during boreal summer.

As in boreal spring, sensible heat fluxes do not play a significant role in comparison with latent heat fluxes in the heat budget of the sea surface (not shown). Reduced surface shortwave radiation is collocated with the positive rainfall anomalies over the north Indian Ocean and the SEIO, providing once again a negative feedback on the positive SST anomalies off the coast of Java (not shown).

iv) Boreal fall and winter

During fall, the SST and rainfall coupled perturbation reaches the equator, propagates westward and gains high significance while weak negative rainfall anomalies appear to the west, north and south of the equator, suggesting a negative IODM rainfall pattern (Figs. 7d and 8d). Furthermore, significant westerly zonal wind anomalies are now locked to the coast of Sumatra suggesting that a positive equatorial wind-thermocline-SST feedback do now contribute to the persistence of the coupled perturbation (Spencer et al., 2005; Fischer et al., 2005).

From November to February, the SST-rainfall perturbation decays significantly and propagates southward (Figs. 7e, f). By January-February, the whole tropical Indian Ocean is covered by weak negative SST anomalies consistent with the positive ISM rainfall simulated during the previous boreal summer (Terray, 1995; Babu and Joseph, 2002). In other words, the air-sea perturbation fades away in late fall or early boreal winter when seasonal wind over the eastern Indian Ocean turns from southeasterly to northwesterly. Since the positive feedback from the wind onto the SST requires a southeasterly basic state (Nicholls, 1979; Hendon, 2003; Wu and Kirtman, 2005), the timing of the onset of the climatological northwesterly winds over the SEIO in the coupled GCM should terminate the positive wind-evaporation-SST feedback over this area. After the reversal of the monsoon wind, the enhanced rainfall due to the warmer SST will generate westerly wind anomalies as before. However, these anomalies now increase the total wind speed along the coast of Sumatra due to the reversal of the wind direction. The induced enhancement of evaporation (Fig. 9f) and upper-ocean mixing will provide now a negative feedback to reduce SST differences consistent with the simulated SST perturbations in Fig. 7f. Thus, the persistence of the coupled perturbation strongly depends on the seasonal evolution of the wind field over the Indian Ocean, highlighting again the importance of the wind-evaporation-SST feedback in our sensitivity experiments.

b. No El Niño composites

Since we are primarily interested in Indian Ocean interactions, a composite has also been created by excluding the strong El Niño years (e.g. a year is excluded if the December-January Niño-3.4 SST anomaly at the end of the year is greater than one standard-deviation). This leaves 31 years with negative, neutral or weak Niño-3.4 anomalies for computing composite differences. The SST, 850 hPa wind and rainfall composites excluding strong El Niño years are shown in Figures 10 and 11, respectively. The seasonal evolution of the

differences are broadly consistent with the previous analysis. This demonstrates that the life cycle of the SEIO coupled perturbation is a manifestation of Indian Ocean interactions and is not significantly influenced by El Niño events or model errors in the Pacific (see section 3).
As above, the slow evolution of the warm SST differences is striking. The core of the warm anomaly decreases in intensity and area, moves northward from off the Australian coast to off the Java coast during spring and summer, then off the Sumatra coast by September-October (Figs. 10a-d). However, some new and interesting features emerge from this composite. First, the amplitude and significance of the SST and rainfall differences are higher in the SEIO across the seasons, suggesting that the positive feedbacks are more active during the years included in this composite. To illustrate this, we observed that a significant low-level cyclonic circulation is now collocated with the positive coupled SST and rainfall perturbation off the west coast of Australia by May-June (Fig. 11b). The amplitude of the collocated (positive and negative) SST and rainfall differences strengthens during boreal summer in this analysis. Other important features to be recognized are enhanced ISM rainfall due to increased latent heat fluxes in the center of the basin during boreal summer and the emergence of more significant IODM SST, low-level wind and rainfall patterns by September-December of this «□No El Niño□ composite (Figs. 10d-f). These IODM patterns are only barely significant during boreal fall in the previous analysis due to the weakness of the anomalies to the west. The physical processes responsible of this stronger interannual variability will be discussed in the framework of the next composite which is constructed from a subset of the «□No El Niño□ years considered here.

c. Warm SEIO composites

Both the efficiency of the wind-evaporation-SST feedback and the intensity of convection increase rapidly with a warmer mean SST. This is due to the nonlinearity of the Clausius-Clapeyron equation which implies that a given SST perturbation may induce larger differences in the atmospheric moisture when the SST background state is warmer. This leads to the hypothesis that the SST-induced atmospheric perturbation described above can be greatly amplified through ocean-atmosphere and circulation-heating interactions when the SST initial state to which we superimpose a SEIO SST perturbation is warmer. In order to test this hypothesis, the differences between the warm and cold SEIO SST perturbation experiments were recomputed for the years when the February-March SEIO SST anomaly

exceeds 0.5 standard-deviation in the control simulation. This selecting criteria leaves a composite of 13 years with a warm SEIO background state in order to test the role of the nonlinear dependence of the evaporation on the SST via the Clausius-Clapeyron relation for the simulated climatic anomalies. The SST, 850 hPa wind, rainfall, evaporation statistics for this particular group of years are presented in Figures 12-14, respectively. Note that similar results are obtained if the differences are computed for the years when the (February-March) Niño3 or Niño-3.4 SST anomaly exceeds a 0.75 or 1 standard-deviation threshold in the control simulation. This is due to the enhanced ENSO-Indian Ocean teleconnexion which is typical of this coupled GCM. In other words, a warm SEIO SST anomaly during February-March indicates that the preceding year was an El Niño year due to the overestimated ENSO variability in this coupled GCM. Thus, the years included in this composite are a subset of the years selected in the previous «□No El Niño□» analysis.

As expected, the warmer SEIO basic state leads to an enhanced seasonally positive wind-evaporation-SST feedback due to the nonlinear dependence of the evaporation from the ocean on the total SST. Higher evaporation differences are observed during May-June in this composite (Fig. 14b). In turn, this enhanced evaporation anomaly has a more significant impact on atmospheric humidity and, hence, convection in the SEIO area as suggested by the enhanced precipitation which overlies the warm SST anomaly during spring and early summer (Figs. 13a, b). Consistent with this hypothesis, there are also significantly enhanced cyclonic wind differences over the SEIO which contribute to enhanced evaporation, oceanic mixing and entrainement differences. Thus, the stronger atmospheric response feeds back positively onto the ocean, leading to a quick growth of the coupled ocean-atmosphere perturbation during spring and early boreal summer.

It is also noteworthy, that SST, 850 hPa wind and rainfall differences are now insignificant farther west contrary to what happens in the first two composites during May-June (Figs. 12b and 13b). Furthermore, there is only a weak ISM response during May-June (more consistent with the observations) in comparison to the previous composites which suggested a delayed ISM onset (Figs. 8b and 11b).

All these features suggest that the atmospheric anomalies triggered by the initial SEIO temperature perturbation favor both the growth and northeastward propagation of the coupled perturbation. This highlights the importance of the SST background state for the strength of the positive wind-evaporation-SST feedback in this coupled GCM.

During July-August, enhanced precipitation is simulated over the warm SEIO SST anomaly and, also, over the Arabian Sea, the Indian subcontinent and the Bay of Bengal (Fig. 13c). Comparison with the first composites indicates that, although the locations of the precipitation anomalies during the boreal summer are the same, the positive precipitation anomalies are stronger in this composite (1.5 to 2 mm day^{-1}). As in the first composites, the direction of the anomalous winds indicates enhanced wind speed over the core region of the trade-winds in the south Indian Ocean (Fig. 13c). Thus, the enhanced wind speed implies that ocean mixing and evaporation are intensified (Fig. 14c). Furthermore, significant positive evaporation differences are now observed to the north of the equator. These features indicate the significant contribution from the wind to the SST tendency over the whole Indian Ocean. This anomalous moisture can then feed «downstream» portions of the monsoon system.

The IODM SST, rainfall and low-level wind patterns gain also significance in this composite (Figs 12d and 13d). Interestingly, this significant negative IODM pattern is preceded by significant northwesterly wind differences locked to the coasts of Java and Sumatra during boreal spring and early summer. Once again, these wind anomalies to the south of the equator were not significant in the previous composites during May-June (see Figs. 8b and 11b). These persistent northwesterly wind anomalies may then contribute to the stronger IODM variability via decreased ocean mixing and coastal upwelling as the wind anomalies are aligned against the mean wind in these areas. This is in agreement with several recent studies which highlight the key-role of southeasterly wind anomalies along the coasts of Sumatra and Java for triggering positive IODM events (Xie et al., 2002; Gualdi et al., 2003; Spencer et al., 2005; Fischer et al., 2005; Behera et al., 2006).

During July-August, the SST composites show warm SST differences in the southeast and cold SST differences farther west, suggesting the rapid growth of the SST dipole pattern (Fig. 12c). The evaporation composite shows a significant west-east contrast just south of the equator as in the previous composites (Fig. 14c). However, highly significant positive evaporation differences are now collocated with the warmer SST anomalies locked to the coast of Java during July-August. Thus, the latent heat flux provides a negative feedback on the warm SST anomaly off Java at this stage of the evolution of the coupled perturbation. This confirms the key role of ocean dynamics (e.g. the coastal upwelling or entrainment feedback off Java and Sumatra) in the persistence of the warm SST perturbation from boreal summer to

fall in this composite since the shortwave radiation also provides a negative feedback on SST in this region (not shown).

Interestingly, the sensible heat flux is now an important process for cooling the SST in the center of the basin, in addition to the enhanced evaporation, during boreal summer (not shown). The stronger trade-winds to the south of the equator seem to advect «□old□, higher-latitude air and these temperature anomalies are communicated to the ocean via the surface sensible heat fluxes (sensible cooling of 2-3 W/m^2). Thus, the latent and sensible heat fluxes work together to cool the sea surface in the center of the basin (Fig. 12c). A reversed mechanism seems at work farther east (near 100°E and 10°S) since the negative evaporation anomalies are larger in these regions in the present composite compared to those observed in the first analyses (Fig. 14c). This feature is also in agreement with the low-level cyclonic circulation observed over the SEIO during the whole summer in this composite (Fig. 13c).

During September-October, the IODM SST pattern reaches its peak (Fig. 12d). Furthermore, the SST dipole is now accompanied by collocated rainfall anomalies (Fig. 13d). The warm SST anomalies in the southeast have strengthened considerably and propagate westward along the equator despite the negative feedback of the evaporation (e.g. latent heat cooling) on the SST along the Sumatra coast during September-October (Fig. 14d). Interestingly, the cold SST differences in the west are stronger and significant south of the equator. This is consistent with the large surface fluxes and advection differences associated with the strengthening of the southeasterly trade-winds in the center of the basin (south of the equator) during boreal summer. This feature is also in good agreement with the evolution of IODM events that are not accompanied by strong El Niño events (Saji and Yamagata, 2003□Spencer et al., 2005). By contrast to what is observed during July-August, the 850 hPa wind composite shows a highly significant weakening of the southeasterly climatological winds off Sumatra and large westerly wind anomalies along the equator during September-October (Fig. 13d, e.g. the northwesterly wind anomalies have moved northward). This suggests the beginning of the positive wind-thermocline-SST feedback along the equator, and of the coastal upwelling feedback farther east, off the coast of Sumatra, since the latent heat flux provides a negative feedback on SST off Sumatra during fall (Fig. 14d). This demonstrates again the role of ocean dynamics at this stage of the coupled perturbation. On the other hand, the southeasterly wind anomalies in the center of the basin weaken and are deflected to the east during September-October (Fig. 13d).

In November-February, after the peak of IODM, the warm anomalies in the southeast move southward and decay to insignificant values (Figs. 12e, f). The cold anomalies farther west decay also during late boreal fall. By January-February, the whole tropical Indian Ocean is covered by significant negative SST differences consistent with the stronger ISM rainfall response observed during the previous boreal summer in this composite. The decay of the warm SST differences in the SEIO is again contemporaneous with the reversal of the climatological monsoon winds as in the first composites.

5. Discussion and conclusions

Previous observational studies have shown that boreal winter SEIO SST anomalies induced by Mascarene high pulses exhibit significant relationships with the evolution of the whole monsoon-ENSO-IODM system. It was suggested that the positive wind-evaporation-SST and wind-thermocline-SST feedbacks in the SEIO and off the Java-Sumatra coast could support these SST anomalies, thus providing a one-year memory for the SST signal and allowing its northward propagation across the seasons. This very long memory may then explain why SEIO SSTs are a highly significant precursor of transitions of the whole monsoon-ENSO-IODM system during recent decades. However, these observational studies only allow identification of common structures in time and space between different variables and are only suggestive of the physical processes involved. Consequently, the role of SEIO SST anomalies in the evolution of the monsoon-ENSO-IODM system has been studied here by using a state-of-the-art coupled GCM.

In a preliminary step, the skill of the CNRM coupled model to simulate the Indo-Pacific climate has been assessed. The CNRM model simulates the mean characteristics of the Asian-Australian monsoon reasonably well. However, the CNRM model has significant errors in equatorial Pacific SST, low-level winds and precipitation, as many other coupled models without flux adjustment (AchutaRao and Sperber, 2002). The simulated ENSO mode is too strong, too regular (3-yr periodicity) and extends too westward in the Pacific and Indian oceans warm pool. Consistent with the higher ENSO variability, the Indian Ocean teleconnection has become stronger through the tropical atmospheric bridge mechanism. In particular, these model biases lead to incorrect representations of the SEIO SST variability during boreal winter and reduce the influence of Mascarene high pulses that partially drive the observed SST variations in this region. However, the model captures many aspects of the

observed ISM-ENSO and Indian Ocean SST-ENSO relationships. Significant cold tropical Indian Ocean SST anomalies lead the El Niño signal by about one or two seasons, consistent with observations after the 1976-77 climate shift (Terray and Dominiak, 2005). Furthermore, an IODM pattern and a basin-wide Indian Ocean warming appear, respectively, in the fall and winter of ENSO developing years as in the observations. The Indian ocean SST anomalies affect the ENSO transitions through modulation of convective heating over the Indian Ocean and of the Indo-Pacific Walker circulation during spring. Cold (warm) Indian Ocean SST anomalies induce westerly (easterly) low-level zonal wind anomalies over the western equatorial Pacific in the control simulation. These wind anomalies may then enhance the reversed phase of the simulated ENSO mode through thermocline fluctuations and oceanic advection. Thus, Indian Ocean variability may induce changes in the Pacific Ocean through this mechanism in agreement with several recent studies (Watanabe and Jin, 2002; Meehl et Arblaster, 2002a; Wu and Kirtman, 2004b; Annamalai et al., 2005b). However, this mechanism does not agree well with the observations after 1976-77 (Terray et al., 2005b; Terray and Dominiak, 2005); it is partly related to the regularity of the ENSO mode in the control simulation while ENSO has a longer and broader period and is thus less regular after 1976-77 in the observations.

This hypothesis that SEIO SST anomalies can influence the evolution of the monsoon-ENSO-IODM system has then been tested in additional coupled numerical experiments. More precisely, we performed ensembles of short integrations with specified SEIO temperature forcing inserted in the February restarts of the fully coupled CNRM model in order to assess the influence of SEIO SST anomalies on the monsoon-ENSO-IODM system despite the model biases. For each year of the control simulation, the coupled model was then integrated for a one-year period for both 1°K warm and cold SEIO perturbations. These sensitivity experiments first confirm that, an SEIO SST perturbation generated during late boreal winter can be maintained and, eventually, amplified through various positive air-sea feedbacks (e.g. wind-evaporation-SST, coastal upwelling and equatorial wind-thermocline-SST feedbacks) until the following boreal fall (Terray et al., 2005b; Terray and Dominiak, 2005).
Furthermore, these sensitivity tests confirm that boreal winter SEIO SSTs anomalies can serve as a triggering mechanism for IODM variability several months later. The SEIO temperature perturbation has also a significant impact on ISM variability. The rainfall patterns differences between the warm and cold SEIO experiments strongly support the hypothesis that SEIO SST

is modulating the ISM system in boreal summer. Precipitation over India increases (decreases) during warm (cold) SEIO years as observed (Terray et al., 2003). Interestingly, the composite difference fields show that the enhanced ISM rainfall cannot be attributed to a strengthening of the monsoon circulation over the north Indian Ocean, but to enhanced evaporation over the south Indian Ocean. These latent heat fluxes are induced by the stronger southeasterly trade winds which form the west branch of the anomalous cyclonic circulation associated with the SEIO SST perturbation. This shows that positive ISM rainfall anomalies over the Indian subcontinent and adjoining oceanic areas could occur in response to increased moisture transport without any significant strengthening of the monsoon circulation over the North Indian Ocean. This result is consistent with observational studies which suggest that 70% of the climatological water vapor transport to the Indian subcontinent by the boreal summer monsoon originates from the south of the equator (Cadet and Reverdin, 1981). In another context, several studies have also suggested that the assumed equivalence between the dynamical and hydrological responses of the monsoon system (e.g. a stronger ISM circulation is equivalent to enhanced precipitation) is questionable (Kitoh et al., 1997; Ashrit et al., 2003).

However, the simulated ENSO mode does not react significantly to the SEIO temperature perturbation in the sensitivity experiments even though the simulated Pacific pattern agrees with the observations during boreal fall. These discrepancies with the observations may be linked to model biases in the Pacific and to the too regular and too strong ENSO simulated by this coupled GCM. In this context, it will be interesting to repeat the sensitivity experiments with other coupled GCMs, particularly those simulating a more realistic ENSO amplitude (e.g. a less strong ENSO mode).

Our results suggest that Indian Ocean has its own modes of coupled variability that are independent of ENSO or model errors since there is a substantial strengthening of the SEIO-ISM-IODM teleconnection when El Niño years are excluded from the composite analysis. Further restricting the composite analysis to the warm SEIO years in the control simulation shows even more significant IODM and ISM responses. One explanation for this increased SST and atmospheric coupled signal may lie in the warmer background state in the SEIO which is characteristic of the years selected in this composite. Due to the non-linearity of the Clausius-Clapeyron equation, a given SST perturbation may provoke larger differences in the atmospheric moisture when the SST background state is warmer. Thus, the SST-induced

atmospheric perturbation is greatly amplified through ocean-atmosphere interactions when the SST initial state onto which we superimpose a SEIO SST perturbation is warmer. Terray and Dominiak (2005) found that the warmer mean state in the SEIO after the 1976-77 regime shift caused interannual variability in the region to increase via enhanced ocean-atmosphere interactions. The current work confirms their results that the variability of tropical oceans is very sensitive to the mean state.

Finally, the present findings suggest that coupled atmosphere-ocean processes are extremely important in the ISM region. Furthermore, it has significant implications for the seasonal predictability of both ISM and IODM events since they demonstrate that the southern Indian Ocean SSTs play an active role in contributing to ISM interannual variability and may trigger IODM events, independent of ENSO-induced variability (Terray et al., 2003; Lau and Nath, 2004; Fischer et al., 2005). However, while we have stressed the importance of SEIO SST anomalies during boreal winter for the monsoon-IODM variability, we did not address the important question of what actually causes these anomalies and this question merits further study.

These results are also in agreement with several recent modeling studies which show that the ISM and, more generally, rainfall variations over the Indo-Pacific warm pool areas cannot be simulated correctly by prescribing lower boundary forcing (Sperber and Palmer, 1996; Wu and Kirtman, 2005; Kumar et al., 2005; Wang et al., 2005; Douville 2005). Predicting or simulating the ISM is a fully coupled ocean-atmosphere problem which must be investigated with coupled GCMs.

Acknowledgments

This work was supported by the French Programme National d'Etude Du Climat (PNEDC) through the VIMA project and the European Community project ENSEMBLES. Sebastien Masson provided graphical software (SAXO) for plotting the results. The authors thank the anonymous reviewers which suggestions improved the original manuscript.

References

AchutaRao, K., and K.R. Sperber, 2002: Simulation of the El Niño Southern Oscillation: Results from the Coupled Model Intercomparison Project. *Clim. Dyn.*, 19, 191-209.

Annamalai, H., S.P. Xie, J.P. McCreary and R. Murtugudde, 2005a: Impact of Indian Ocean sea surface temperature on developing El Niño. *J. Climate*, 18, 302-319.

Annamalai, H., P. Liu, and S.P. Xie, 2005b: Southwest Indian Ocean SST variability: its local effect and remote influence on Asian monsoons. *J. Climate*, 18, 302-319.

Ashok, K., Z. Guan, and T. Yamagata, 2001: Impact of the Indian Ocean dipole on the relationship between the Indian monsoon rainfall and ENSO. *Geophys. Res. Lett.*, 28, 4499-4502.

Ashok, K., Z. Guan, N.H. Saji and T. Yamagata, 2004: Individual and combined influences of ENSO and the Indian Ocean Dipole on the Indian Summer Monsoon. *J. Climate*, 17, 3141-3155.

Ashrit, R.G., H. Douville and K. Rupa Kumar, 2003: Response of the Indian monsoon and ENSO-monsoon teleconnection to enhanced greenhouse effect in the CNRM coupled model. *J. Meteor. Soc. Japan*, 81, 779-803.

Babu, C.B., and P.V. Joseph, 2002: Post-monsoon sea surface temperature and convection anomalies over Indian and Pacific Oceans. *Int. J. Climatol.*, 22, 559-567.

Behera, S.K., and T. Yamagata, 2001: Subtropical SST dipole events in the southern Indian Ocean. *Geophys. Res. Lett.,* 28, 327-330.

Behera, S. K., and T. Yamagata, 2003: Impact of the Indian Ocean Dipole on the Southern Oscillation. *J. Meteor. Soc. Japan*, 81, 169-177.

Behera, S. K., J.J. Luo, S. Masson, P. Delecluse, S. Gualdi, A. Navarra and T. Yamagata, 2005: Paramount impact of the Indian Ocean Dipole on the East African short rains: A CGCM study. *J. Climate*, 18, 4514-4530.

Behera, S. K., J.J. Luo, S. Masson, S.A. Rao and H. Sakuma, 2006: A CGCM study on the interaction between IOD and ENSO. *J. Climate*, 19, 1688-1705.

Cadet, D.L., and G. Reverdin, 1981: Water vapor transport over the Indian Ocean during summer 1975. *Tellus*, 33, 476-487.

Camberlin, P., F. Chauvin, H. Douville and Y. Zhao, 2004: Simulated ENSO-tropical rainfall teleconnections in present-day and under enhanced greenhouse gases conditions. Clim. Dyn., 23, 641-657. DOI 10.1007/s00382-004-0460-7.

Chang, C.P., and T. Li, 2000: A theory for the tropical tropospheric biennial oscillation. *J. Atmos. Sci.*, 57, 2209-2224.

Cherchi, A., S. Gualdi, S. Behera, J.J. Luo, S. Masson, T. Yamagata and A. Navarra, 2006: The influence of tropical Indian Ocean SST on the Indian summer monsoon. *J. Clim.*, in press.

Davison, A. C., and D. V. Hinkley (1997), Bootstrap methods and their application, Cambridge University Press, Cambridge, UK, pp 582.

Déqué, M., C. Dreveton, A. Braun and D. Cariolle, 1994: The ARPEGE/IFS atmosphere model: a contribution to the French community climate modelling. *Clim. Dyn.*, 10, 249-266.

Dominiak, S. and P. Terray, 2005: Improvement of ENSO prediction using a linear regression model with a Southern Indian Ocean Sea Surface Temperature Predictor. *Geophys. Res. Lett.*, 32, L18702, doi:10.1029/2005GL023153.

Douville, H., F. Chauvin, J-F. Royer, S. Salas-Mélia, and S. Tyteca, 2002: Sensitivity of the hydrological cycle to increasing amounts of greenhouse gases and aerosols. *Climate Dyn.*, 20, 45-68.

Douville, H., 2005: Limitations of time-slice experiments for predicting regional climate change over South Asia in the CCM. *Climate Dyn.*, 24, 373-391.

Fischer, A.S., P. Terray, P. Delecluse, S. Gualdi and E. Guilyardi, 2005: Two Independent Triggers for the Indian Ocean Dipole/Zonal Mode in a Coupled GCM. *J. Climate*, 18, 3428–3449.

Gill, A.E., 1980: Some simple solutions for heat-induced tropical circulation. *Quart. J. Roy. Meteor. Soc.*, 106, 447-462.

Goddard, L., and N. Graham, 1999: Importance of the Indian Ocean for simulating rainfall anomalies over eastern and southern Africa. *J. Geophys. Res.*, 104 (D16), 19 099-19 116

Gualdi, S., E. Guilyardi, A. Navarra, S. Masina and P. Delecluse, 2003: The interannual variability in the tropical Indian Ocean as simulated by a CGCM. *Clim. Dyn.*, 20, 567-582.

Guérémy, J-F., M. Déqué, A. Braun, and J-P. Piedelièvre, 2005□Actual and potential skill of seasonal predictions using the CNRM contribution to DEMETER: coupled versus uncoupled model. *Tellus*, 57A, 308-319.

Guilyardi, E, P. Delecluse, S. Gualdi, A. Navarra, 2003□ Mechanisms for ENSO phase change in a coupled GCM. *J. Clim.*, 16, 1141-1158.

Guilyardi, E, 2006: El Nino-mean state-seasonal cycle interactions in a multi-model ensemble. *Clim. Dyn.*, 26:329-348, DOI: 10.1007/s00382-005-0084-6.

Hendon, H., 2003: Indonesia rainfall variability: impacts of ENSO and local air-sea interaction. *J. Clim.*, 16, 1775-1790.

Kalnay et al., 1996: The NCEP/NCAR 40-Year Reanalysis Project. *Bull. Amer. Meteor. Soc.*, **77**, 437-471.

Kim, K.M., and K.M. Lau, 2001: Dynamics of monsoon-induced biennial variability in ENSO. *Geophys. Res. Lett.*, 28, 315-318.

Kirtman, B.P., 1997: Oceanic Rossby waves dynamics and the ENSO period in a coupled model. *J. Clim.*, 10, 1690-1704.

Kitoh, A., S. Yukimoto, A. Noda and T. Motoi, 1997: Simulated changes in the Asian summer monsoon at times of increased atmospheric CO2. *J. Meteor. Soc. Japan*, 75, 1019-1031.

Kug, J.-S., S.-I. An, F. F. Jin, and I.-S. Kang (2005), Preconditions for El Niño and La Niña onsets and their relation to the Indian Ocean. *Geophys. Res. Lett.*, 32, L05706, doi: 10.1029/2004GL021674.

Kumar, K.K., M. Hoerling, and B. Rajagopalan, 2005: Advancing dynamical prediction of Indian monsoon rainfall. *Geophys. Res. Lett.*, 32, L08704, doi: 10.1029/2004GL021979.

Lau, N.C., and M.J. Nath, 2000: Impact of ENSO on the variability of the Asian-Australian monsoons as simulated in GCM experiments. *J. Climate*, 13, 4287-4309.

Lau N.C. and M.J. Nath, 2003: Atmosphere-Ocean Variations in the Indo-Pacific Sector during ENSO Episodes. *J. Climate*, 16, 3-20.

Lau, N.C., and M.J. Nath, 2004: Coupled GCM simulation of atmosphere-ocean variability associated with zonally asymmetric SST changes in the tropical Indian Ocean. *J. Climate*, 17, 245-265.

Levitus, S., 1982: Climatological Atlas of the world ocean. NOAA professional paper No. 13, 173 pp.

Li, T., C.-W Tham, and C.P. Chang, 2001: A coupled air-sea-monsoon oscillator for the troposheric biennial oscillation. *J. Climate*, 14, 752-764.

Li, T., B. Wang, C.P. Chang and Y.S. Zhang, 2003: A theory for the Indian Ocean Dipole-Zonal Mode. *J. Atmos. Sci.*, 60, 2119-2135.

Lindzen, R.S., and S. Nigam, 1987: On the role of sea surface temperature gradients in forcing low-level winds and convergence in the Tropics. *J. Atmos. Sci.*, 44, 2418-2436.

Loschnigg, J., G.A. Meehl, J.M. Arblaster, G.P. Compo, and P.J. Webster, 2003: The Asian monsoon, the tropospheric biennial oscillation, and the Indian Ocean dipole in the NCAR CSM. *J. Climate*, 16, 1617-1642.

Madec G, P. Delecluse, M. Imbard, and C. Levy, 1998□ OPA version 8.1 ocean general circulation model reference manual. Technical Report, LODYC/IPSL, Note 11, Paris, France, pp 91.

Meehl, G.A., and J. Arblaster, 2002a: The tropospheric biennial oscillation and the Asian-Australian monsoon rainfall. *J. Climate*, 15, 722-744.

Meehl, G.A., and J. Arblaster, 2002b: Indian monsoon GCM sensitivity experiments testing tropospheric biennial oscillation transition conditions. *J. Climate*, 15, 923-944.

Meehl G.A., J.M. Arblaster and J. Loschnigg, 2003: Coupled Ocean-Atmosphere Dynamical Processes in the Tropical Indian and Pacific Oceans and the TBO. *J. Climate*, 16, 2138-2158.

Mitchell, T.D., T.R. Carter, P.D. Jones, M. Hulme and M. New, 2003: A comprehensive set of high-resolution grids of monthly climate for Europe and the globe: the observed record (1901-2000) and 16 scenarios (2001-2100). Submitted to *J. Climate*.

Murtuggude, R., J. McCreary, and A. Busalacchi, 2000: Oceanic processes associated with anomalous events in the Indian Ocean with relevance to 1997-1998. *J. Geophys. Res.*, 105 (C2), 3295-3306.

Nicholls, N., 1979: A simple air-sea interaction model. *Q.J.R. Meteorol. Soc*., 105, 93-105.

Nicholls, N., 1995: All-India summer monsoon rainfall and sea surface temperatures around northern Australia and Indonesia. *J. Climate*, 8, 1463-1467.

Noilhan, J. and J.F. Mahfouf, 1996: The ISBA land surface parameterizations plus cloud optical properties in the ECMWF model. *Mon. Wea. Rev*., 118, 847-873.

Noreen, E.W., 1989 : Computer-intensive methods for testing hypotheses: an introduction. John Wiley & Sons, New York.

Reason, J.C.J., 2002: Sensitivity of the southern African circulation to dipole sea-surface temperature patterns in the South Indian Ocean. *Int. J. Climatol*., 22, 377-393.

Saji, N.H., B.N. Goswami, P.N. Vinayachandran, and T.A. Yamagata, 1999: Dipole Mode in the Tropical Indian Ocean. *Nature*, **401**, 360-363.

Saji N.H, and T. Yamagata, 2003: Structure of SST and Surface Wind Variability during Indian Ocean Dipole Mode Events: COAS Observations. *J. Climate*, 16, 2735-2751.

Salas Mélia, D., 2002: A global coupled sea-ice ocean model. *Ocean Model*., 4, 137-172.

Shinoda, T., M.A. Alexander, H. Hendon, 2004: Remote reponse of the Indian Ocean to interannual SST variations in the tropical Pacific. *J. Climate*, 17, 362-372.

Smith, T.M., and R.W. Reynolds, 2004: Improved Extended Reconstruction of SST (1854-1997). *J. Climate,* **17**, 2466-2477.

Spencer H., R.T. Sutton, J.M. Slingo, M. Roberts and E. Black, 2005: Indian Ocean climate and dipole variability in Hadley Centre Coupled GCMs. *J. Climate*, 18, 2286-2307.

Sperber, K.R., and T.N. Palmer, 1996: Interannual tropical rainfall variability in general circulation model simulations associated with the Atmospheric Model Intercomparison Project. *J. Climate*., 9, 2727-2750.

Terray, P., 1995: Space/Time structure of monsoons interannual variability. *J. Climate*, 8, 2595-2619.

Terray, P., P. Delecluse, S. Labattu, and L. Terray, 2003: Sea Surface Temperature Associations with the Late Indian Summer Monsoon. *Clim. Dyn.*, **21**, 593-618.

Terray P., E. Guilyardi, A.S. Fischer and P. Delecluse, 2005a: Dynamics of the Indian Monsoon and ENSO Relationships in the SINTEX global Coupled Model. *Clim. Dyn.* , 24, 145-168.

Terray P., S. Dominiak and P. Delecluse, 2005b: Role of the southern Indian Ocean in the transitions of the monsoon-ENSO system during recent decades. *Clim. Dyn.*, 24, 169-195, DOI: 10.1007/s00382-004-0480-3.

Terray P. and S. Dominiak, 2005: Indian Ocean Sea Surface Temperature and El Niño-Southern Oscillation: A new perspective. *J. Climate*, 18, 1351-1368.

Turner, A.G, P.M. Inness and J.M. Slingo, 2005: The role of the basic state in the ENSO-monsoon relationship and implications for predictability. *Q.J.R. Meteorol. Soc*., 131, pp. 781-804.

Valcke S, L. Terray, and A. Piacentini, 2000⊡The OASIS coupler user guide version 2.4. Technical Report, TR/CMGC/00-10, CERFACS, Toulouse, France, pp 85

Wallace, J.M., and D.S. Gutzler, 1981: Teleconnections in the geopotential height field during the Northern Hemisphere winter. *Mon. Wea. Rev*., 109, 784-812.

Wang, B., 1995: Interdecadal changes in El Niño onset in the last four decades, *J. Climate*, 8, 267-285.

Wang, B., and S.-I. An, 2001: Why the Properties of El Niño Changed during the Late 1970s. *Geophys. Res. Lett.,* **28**, 3709-3712.

Wang, B., R. Wu and K.-M. Lau, 2001: Interannual variability of the Asian summer monsoon: contrasts between the Indian and the Western North Pacific-East Asian monsoons. *J. Climate*, 14, 4073-4090.

Wang B. and Q. Zhang, 2002: Pacific-East Asian teleconnection. Part II: How the Philippine Sea anomalous anticyclone is established during El Niño development. *J. Climate*, 15, 3252-3265.

Wang, B., R. Wu, and T. Li, 2003: Atmosphere-Warm Ocean Interaction and its Impacts on Asian-Australian Monsoon Variation. *J. Climate*, 16, 1195-1211.

Wang, B., Q. Ding, X. Fu, I.S. Kang, K. Jin, J. Shukla and F. Doblas-Reyes, 2005: Fundamental challenge in simulation and prediction of summer monsoon rainfall. *Geophys. Res. Lett.,* **32**, L15711 doi: 10.1029/2005GL022734.

Watanabe, M., and F.-F. Jin, 2002: Role of Indian Ocean warming in the development of Philippine Sea anticyclone during ENSO. *Geophys. Res. Lett.,* **29**, doi: 10.1029/2001GL014318.

Webster, P.J., V.O. Magana, T.N. Palmer, J. Shukla, R.A. Tomas, M. Yanai, and T. Yasunari, 1998: Monsoons: Processes, predictability and the prospects for prediction. *J. Geophys. Res.* , 103 (C7), 14 451-14 510.

Webster P.J., A.M. Moore, J.P. Loschnigg and R.R. Leben, 1999: Coupled ocean-atmosphere dyniamics in the Indian Ocean during 1997-1998. *Nature*, 401, 356-360.

Webster, P. J., C. Clark, G. Cherikova, J. Fasullo, W. Han, J. Loschnigg, and K. Sahami, 2002: "The Monsoon as a self-regulating coupled ocean-atmosphere system." Meteorology at the Millennium. Academic Press, 198-219.

Wu, R., and B.P. Kirtman, 2004a: Impacts of the Indian Ocean on the Indian summer monsoon-ENSO relationship. *J. Climate,* 17, 3037-3054.

Wu, R., and B.P. Kirtman, 2004b: Understanding the impact of the Indian Ocean on ENSO variability in a coupled GCM. *J. Climate,* 17, 4019-4031.

Wu, R., and B.P. Kirtman, 2005: Roles of Indian and Pacific Ocean air-sea coupling in tropical atmospheric variability. *Clim. Dyn.* , 25, 155-170.

Xie, S.P., H. Annamalai, F.A. Schott and J.P. McCreary, 2002: Structure and Mechanisms of South Indian Ocean Climate Variability. *J. Climate*, 15, 864-878.

Yamagata, T., and coauthors, 2002: The Indian Ocean dipole: A physical entity. *Clivar Exch.*, **7** (2), 15-18.

Yu, J.-Y., S.-P. Weng, and J.D. Farrara, 2003: Ocean Roles in the TBO Transitions of the Indian-Australian Monsoon System. *J. Climate,* 16, 3072-3080.

FIGURE CAPTIONS

Figure 1: February mixed layer depth (in meters) in the Indian Ocean in the control simulation (1950-1998) of the CNRM-CM2 coupled GCM. The SEIO geographical domain used in the sensitivity experiments is indicated by a black frame.

Figure 2: Bimonthly 850 hPa wind, rainfall (panels **a**, **b**, **c**, **d**, **e**, **f**) and SST (panels **g**, **h**, **i**, **j**, **k**, **l**) climatologies as simulated by the CNRM-CM2 model.

Figure 3: **a** Mean annual cycle of rainfall averaged over the Indian subcontinent (land grid points between 5-30°N and 70-95°E) for the observations (CRU dataset) and the coupled model simulation. **b** mean annual cycle of IMDI (see text for explanations) computed from 850 hPa zonal wind from the NCEP reanalysis and from the coupled model simulation.

Figure 4: Bimonthly SST standard-deviations as computed from observations (panels **a**, **b**, **c**, **d**, **e**, **f**) and simulated by the CNRM-CM2 model (panels **g**, **h**, **i**, **j**, **k**, **l**). Contour interval is 0.2 °C.

Figure 5: Time sequence of correlations with December-January Niño3.4 (5°S-5°N/170°-120°W) SST time series of Indo-Pacific SSTs at –5 to 0 bi-monthly seasons computed from the control simulation of the CNRM-CM2 model. Panels **a**-**f** from February-March to December-January before December-January Niño3.4 SST. Correlations that are above the 90% confidence level estimated with a phase-scrambling bootstrap test with 999 samples are shaded.

Figure 6: Time sequence of regression coefficients of Indo-Pacific 850 hPa wind (arrows, see scales below the panels) and rainfall (color shading) versus the December-January Niño3.4 (5°S-5°N/190°-240°E) SST time series at –5 to 0 bi-monthly seasons computed from the control simulation of the CNRM-CM2 model. Panels **a**-**f** from February-March to December-January before December-January Niño3.4 SST. The convention for the color shading is indicated at the bottom of the panels. The maps only show regression coefficients that are above the 90% confidence level following a phase-scrambling procedure with 999 samples.

Figure 7: Bimonthly SST differences between the warm and cold SEIO experiments averaged over all the years (49 years) from March-April before ISM to January-February after ISM (panels **a**, **b**, **c**, **d**, **e**, **f**). Differences significant at the 90% confidence level are shaded. These critical probabilities have been assessed using a permutation procedure with 9999 shuffles.

Figure 8: Same as Figure 7, but for 850 hPa wind and rainfall differences. The maps only show 850 hPa wind differences that are above the 90% confidence level.

Figure 9: Same as Figure 7, but for evaporation differences.

Figure 10: Bimonthly SST differences between the warm and cold SEIO experiments averaged over the «□o El Niño□ years (31 years) from March-April before ISM to January-February after ISM (panels **a**, **b**, **c**, **d**, **e**, **f**). Differences significant at the 90% confidence level are shaded. These critical probabilities have been assessed using a permutation procedure with 9999 shuffles.

Figure 11: Same as Figure 10, but for 850 hPa wind and rainfall differences. The maps only show 850 hPa wind differences that are above the 90% confidence level.

Figure 12: Bimonthly SST differences between the warm and cold SEIO experiments averaged over the «warm SEIO» years (13 years) from March-April before ISM to January-February after ISM (panels **a**, **b**, **c**, **d**, **e**, **f**). Differences significant at the 90% confidence level are shaded. These critical probabilities have been assessed using a permutation procedure with 9999 shuffles.

Figure 13: Same as Figure 12, but for 850 hPa wind and rainfall differences. The maps only show 850 hPa wind differences that are above the 90% confidence level.

Figure 14: Same as Figure 12, but for evaporation differences.

Figure 1

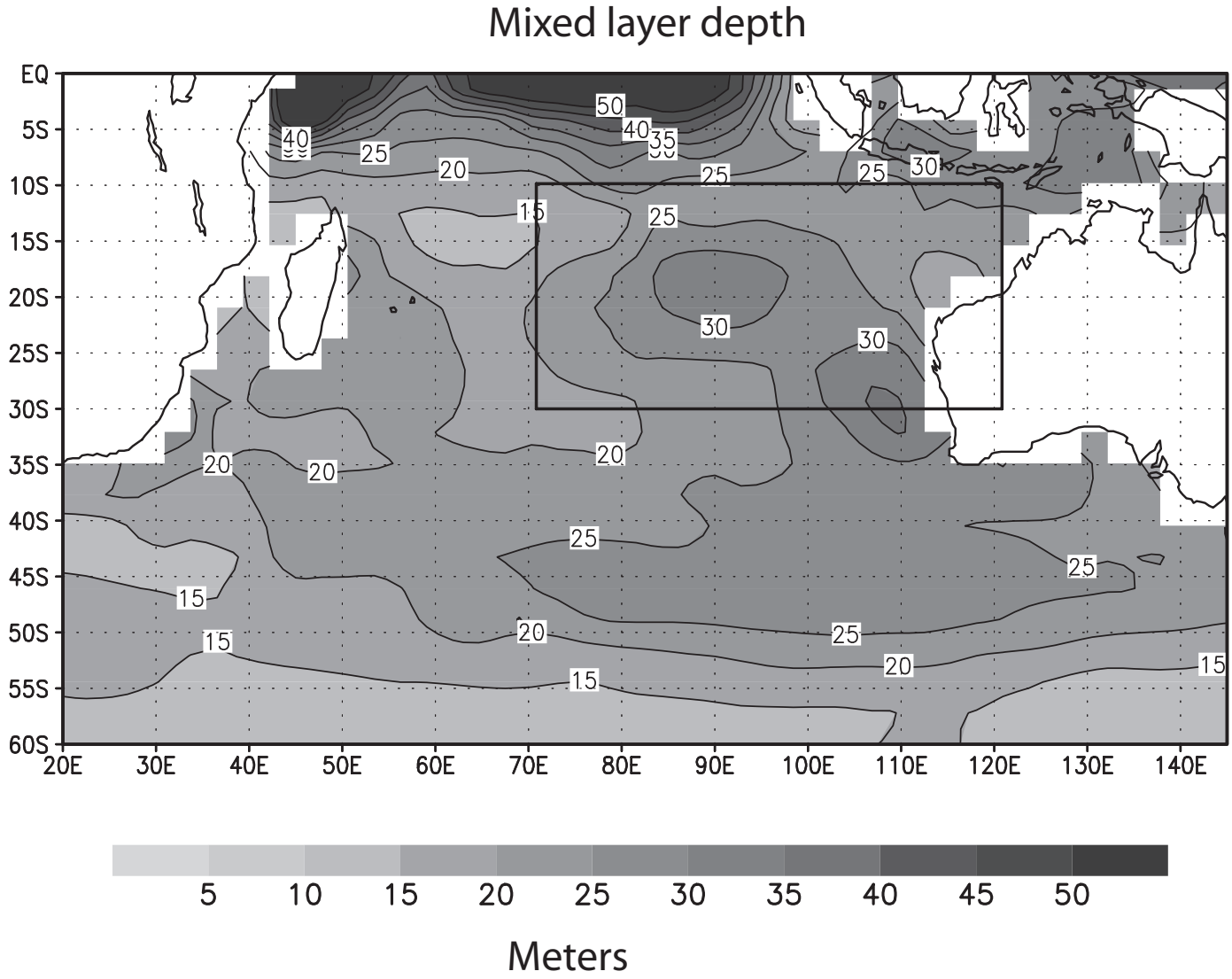
Mixed layer depth
EQ
5S
10S
15S
20S
25S
30S
35S
40S
45S
50S
55S
60S
20E
30E
40E
50E
60E
70E
80E
90E
100E
110E
120E
130E
140E
5
10
15
20
25
30
35
40
45
50
Meters

Figure 2

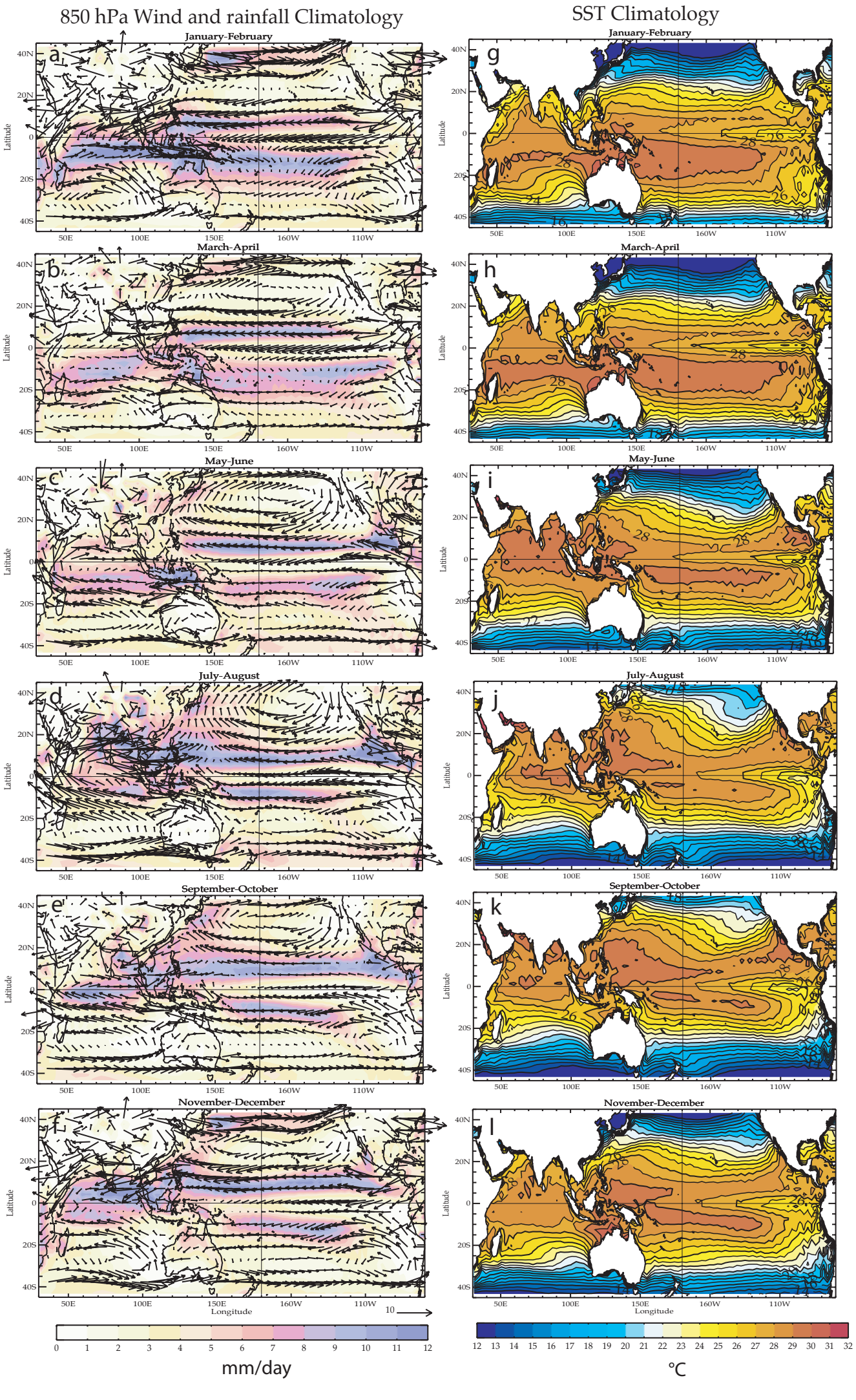
850 hPa Wind and rainfall Climatology
SST Climatology
January-February
March-April
May-June
July-August
September-October
November-December
a
b
c
d
e
f
g
h
i
j
k
l
Latitude
Longitude
40N
20N
0
20S
40S
50E
100E
150E
160W
110W
10
0 1 2 3 4 5 6 7 8 9 10 11 12
mm/day
12 13 14 15 16 17 18 19 20 21 22 23 24 25 26 27 28 29 30 31 32
°C

Figure 3

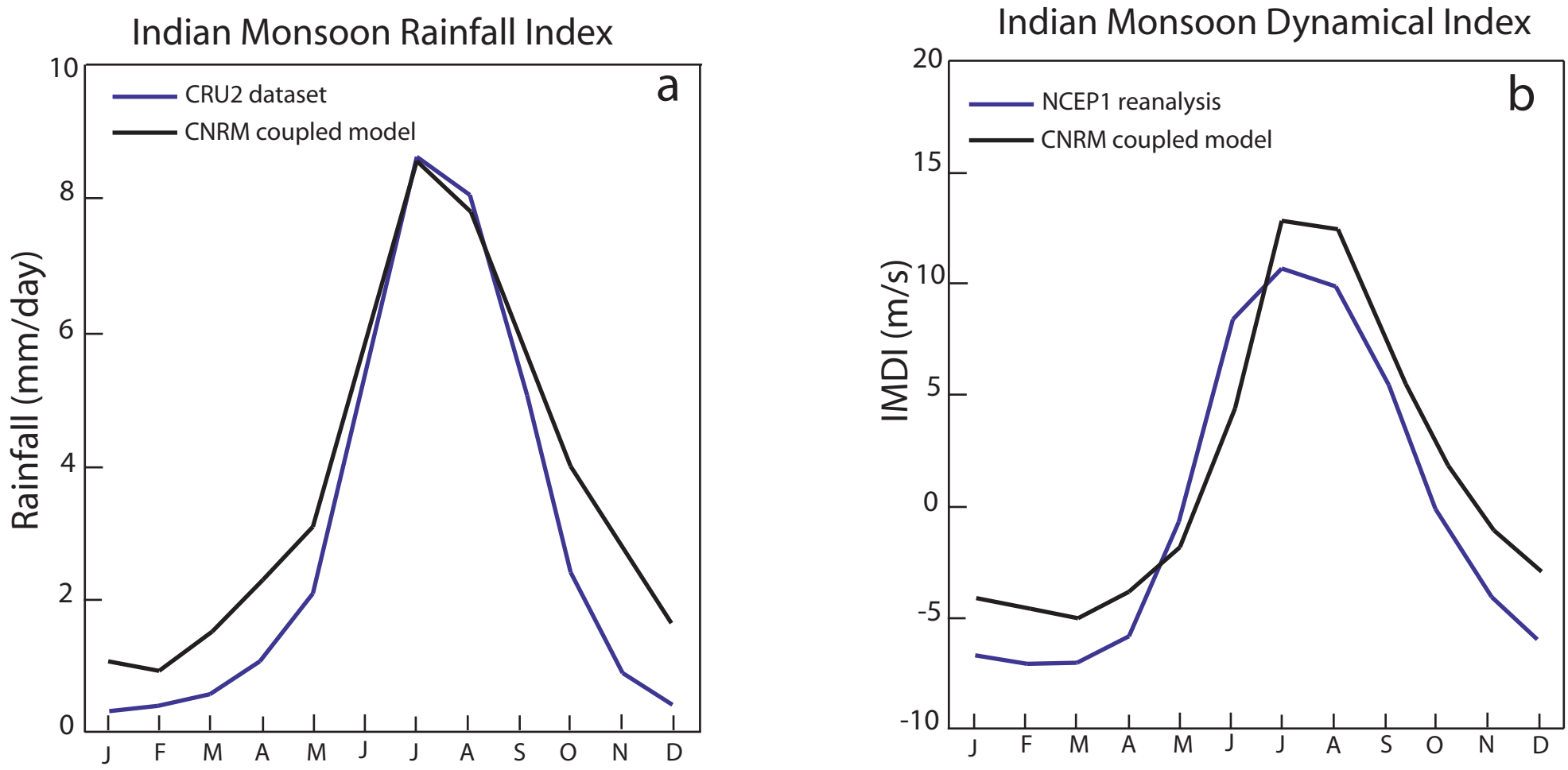
Indian Monsoon Rainfall Index
a
CRU2 dataset
CNRM coupled model
Rainfall (mm/day)
10
8
6
4
2
0
J F M A M J J A S O N D
Indian Monsoon Dynamical Index
b
NCEP1 reanalysis
CNRM coupled model
IMDI (m/s)
20
15
10
5
0
-5
-10
J F M A M J J A S O N D

Figure 4

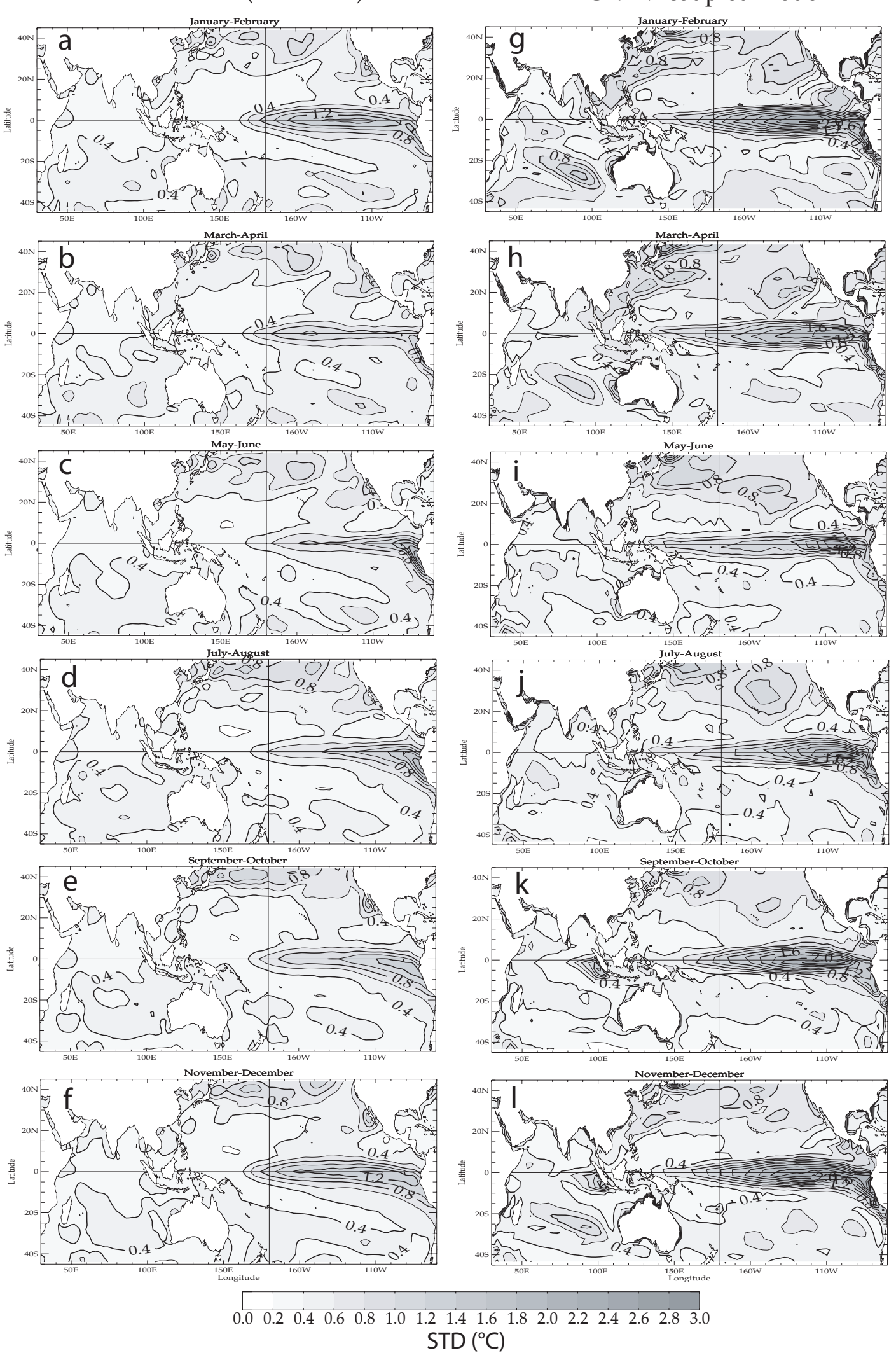
ERSST2 (1950-1998)
CNRM coupled model
January-February
March-April
May-June
July-August
September-October
November-December
a
b
c
d
e
f
g
h
i
j
k
l
Latitude
Longitude
40N
20N
0
20S
40S
50E
100E
150E
160W
110W
0.0 0.2 0.4 0.6 0.8 1.0 1.2 1.4 1.6 1.8 2.0 2.2 2.4 2.6 2.8 3.0
STD (°C)

Figure 5

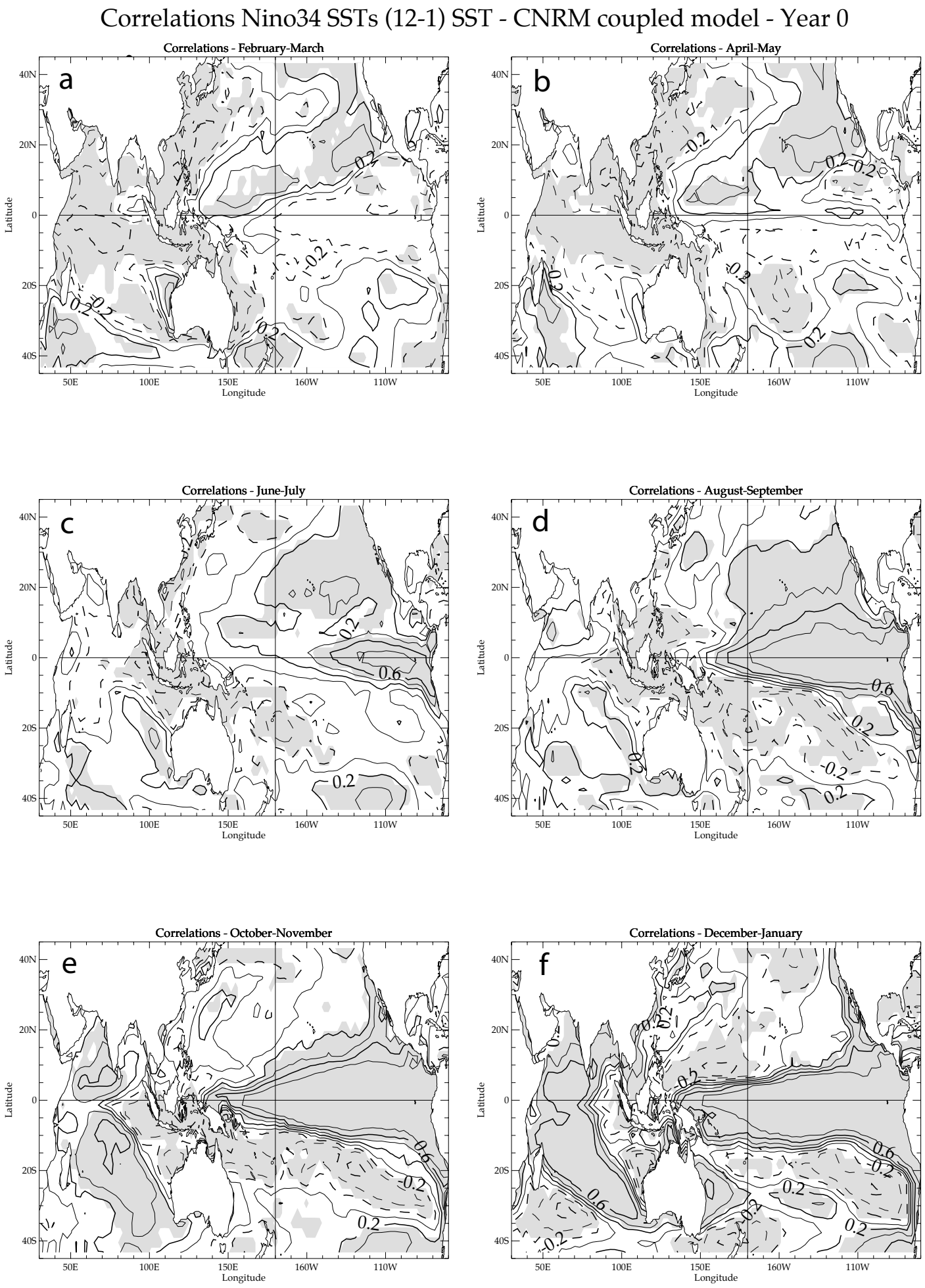
Correlations Nino34 SSTs (12-1) SST - CNRM coupled model - Year 0
Correlations - February-March
a
Correlations - April-May
b
Correlations - June-July
c
Correlations - August-September
d
Correlations - October-November
e
Correlations - December-January
f
Latitude
Longitude
40N
20N
0
20S
40S
50E
100E
150E
160W
110W
0.2
-0.2
0.6

Figure 6

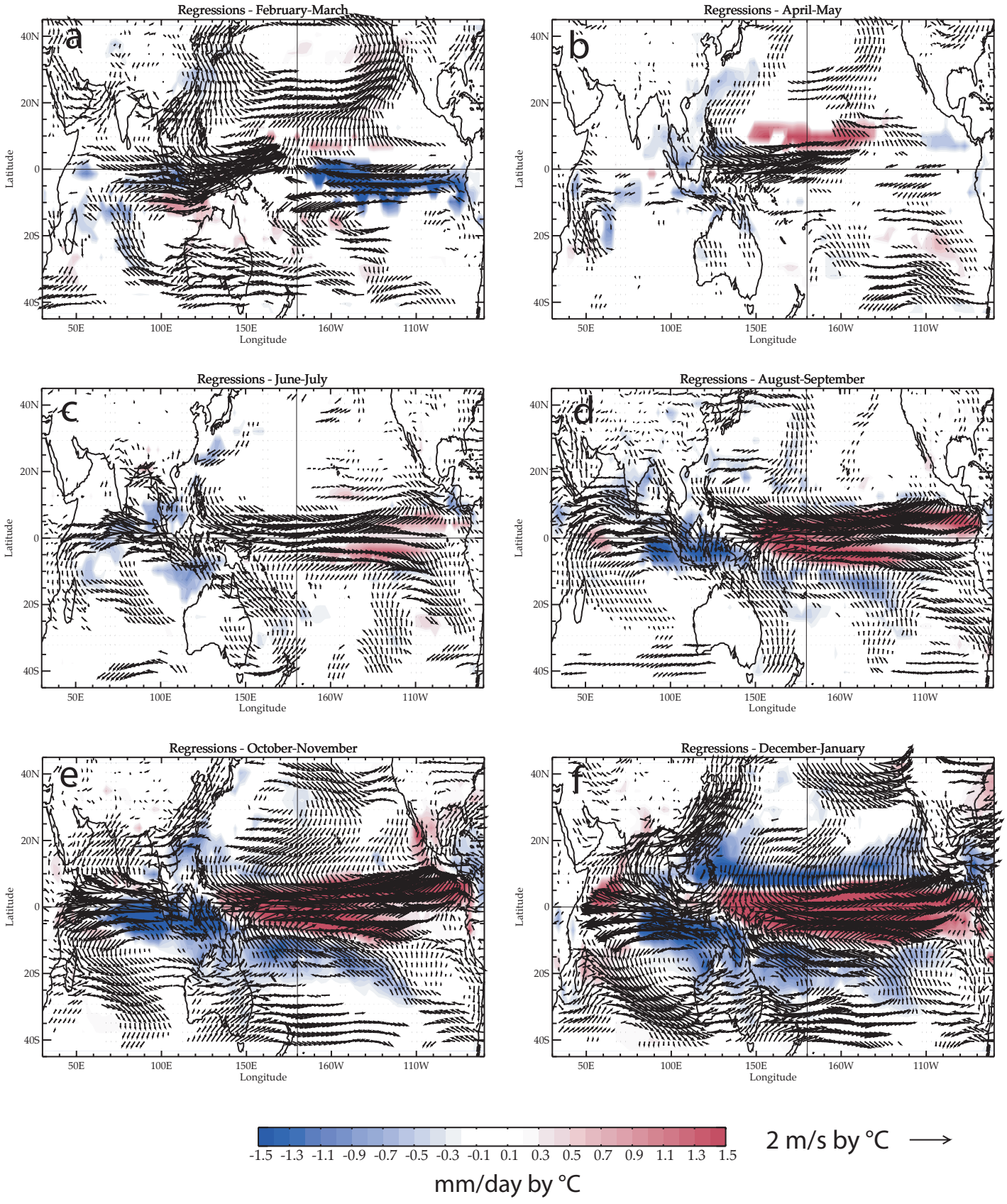
Regressions Nino3.4 SSTs (12-1) 850 hPa wind / rainfall - CNRM coupled model - Year 0
Regressions - February-March
a
Regressions - April-May
b
Regressions - June-July
c
Regressions - August-September
d
Regressions - October-November
e
Regressions - December-January
f
40N
20N
0
20S
40S
Latitude
50E
100E
150E
160W
110W
Longitude
-1.5 -1.3 -1.1 -0.9 -0.7 -0.5 -0.3 -0.1 0.1 0.3 0.5 0.7 0.9 1.1 1.3 1.5
mm/day by °C
2 m/s by °C

Figure 7

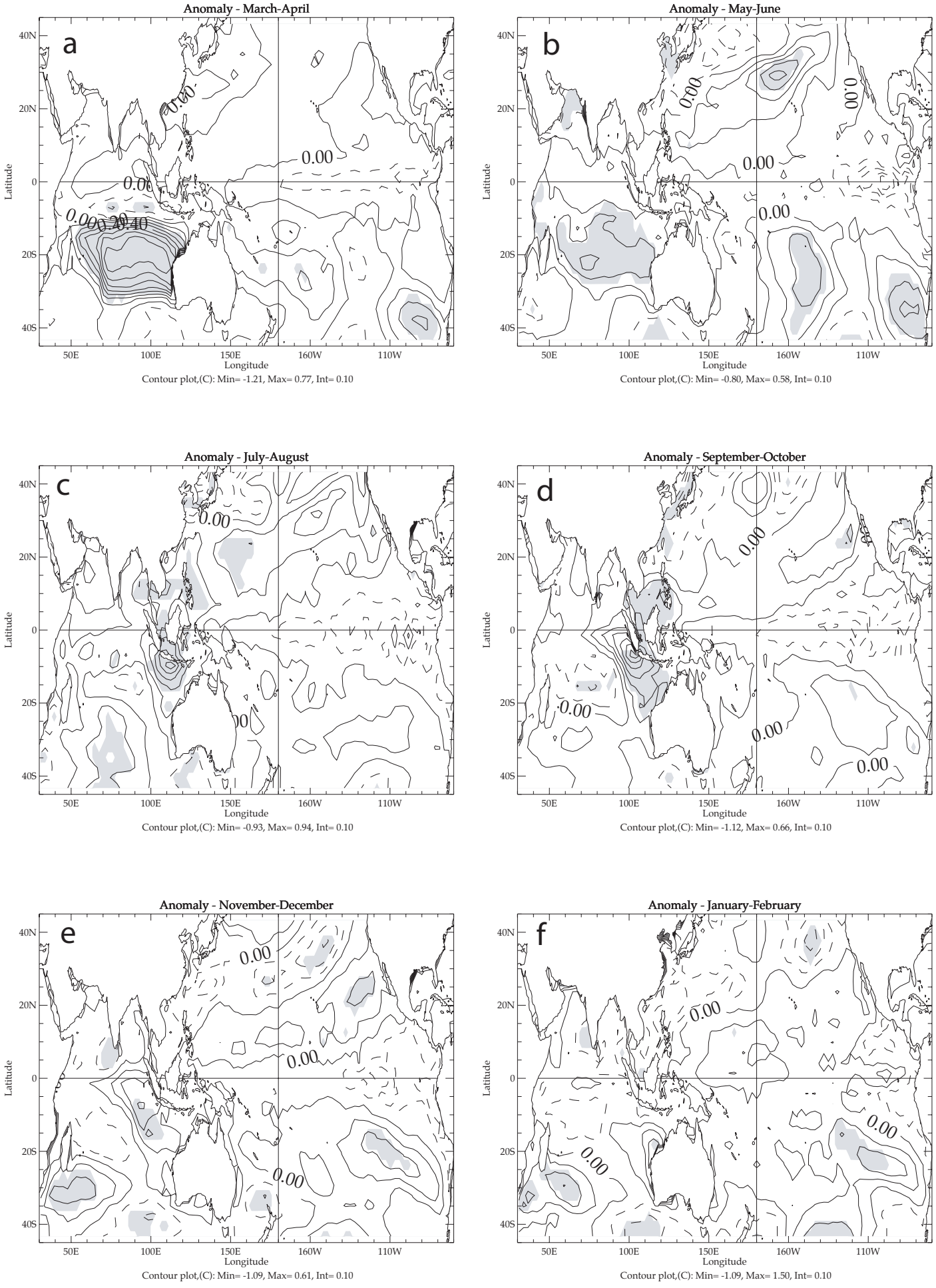
Positive - negative SEIO SST perturbations, SST, (all years) year+1
Anomaly - March-April
a
Contour plot,(C): Min= -1.21, Max= 0.77, Int= 0.10
Anomaly - May-June
b
Contour plot,(C): Min= -0.80, Max= 0.58, Int= 0.10
Anomaly - July-August
c
Contour plot,(C): Min= -0.93, Max= 0.94, Int= 0.10
Anomaly - September-October
d
Contour plot,(C): Min= -1.12, Max= 0.66, Int= 0.10
Anomaly - November-December
e
Contour plot,(C): Min= -1.09, Max= 0.61, Int= 0.10
Anomaly - January-February
f
Contour plot,(C): Min= -1.09, Max= 1.50, Int= 0.10
Latitude
Longitude
40N
20N
0
20S
40S
50E
100E
150E
160W
110W

Figure 8

Positive - negative SEIO SST perturbations, 850 hPa wind and rainfall, (all years) year+1

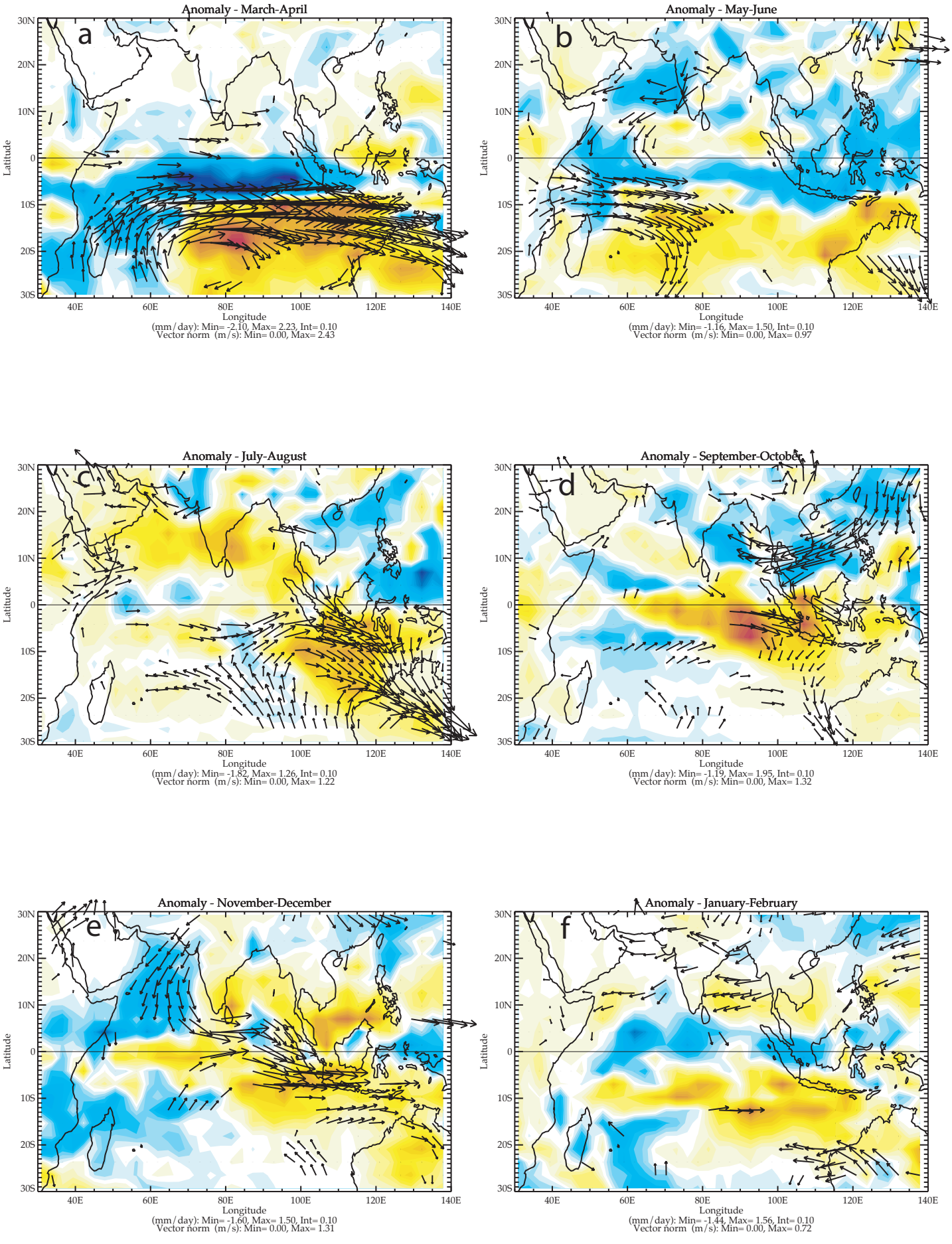

Figure 9

Positive - negative SEIO SST perturbations, Evaporation, (all years) year+1

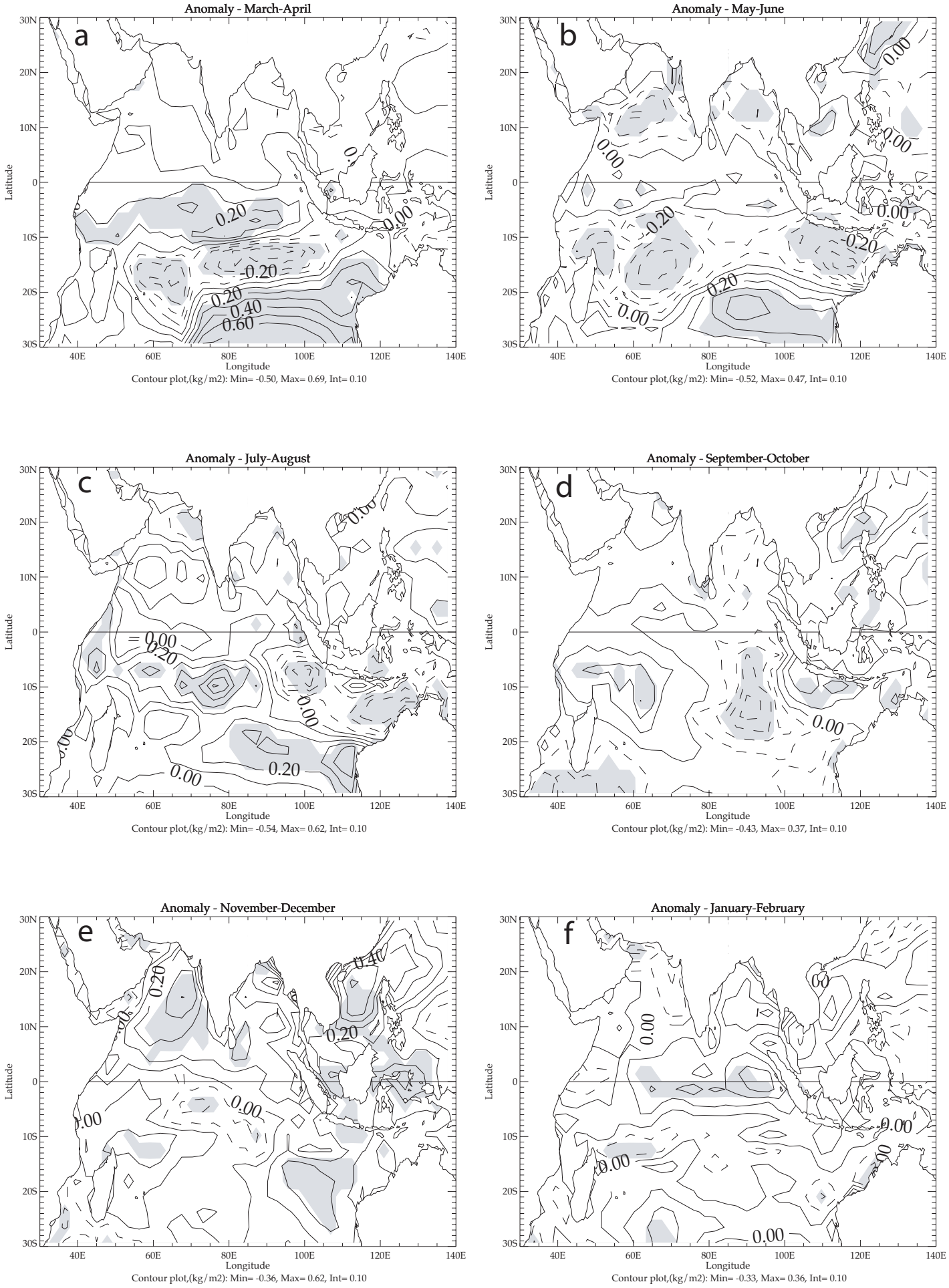

Figure 10

Positive - negative SEIO SST perturbations, SST, (No EL NINO years) year+1

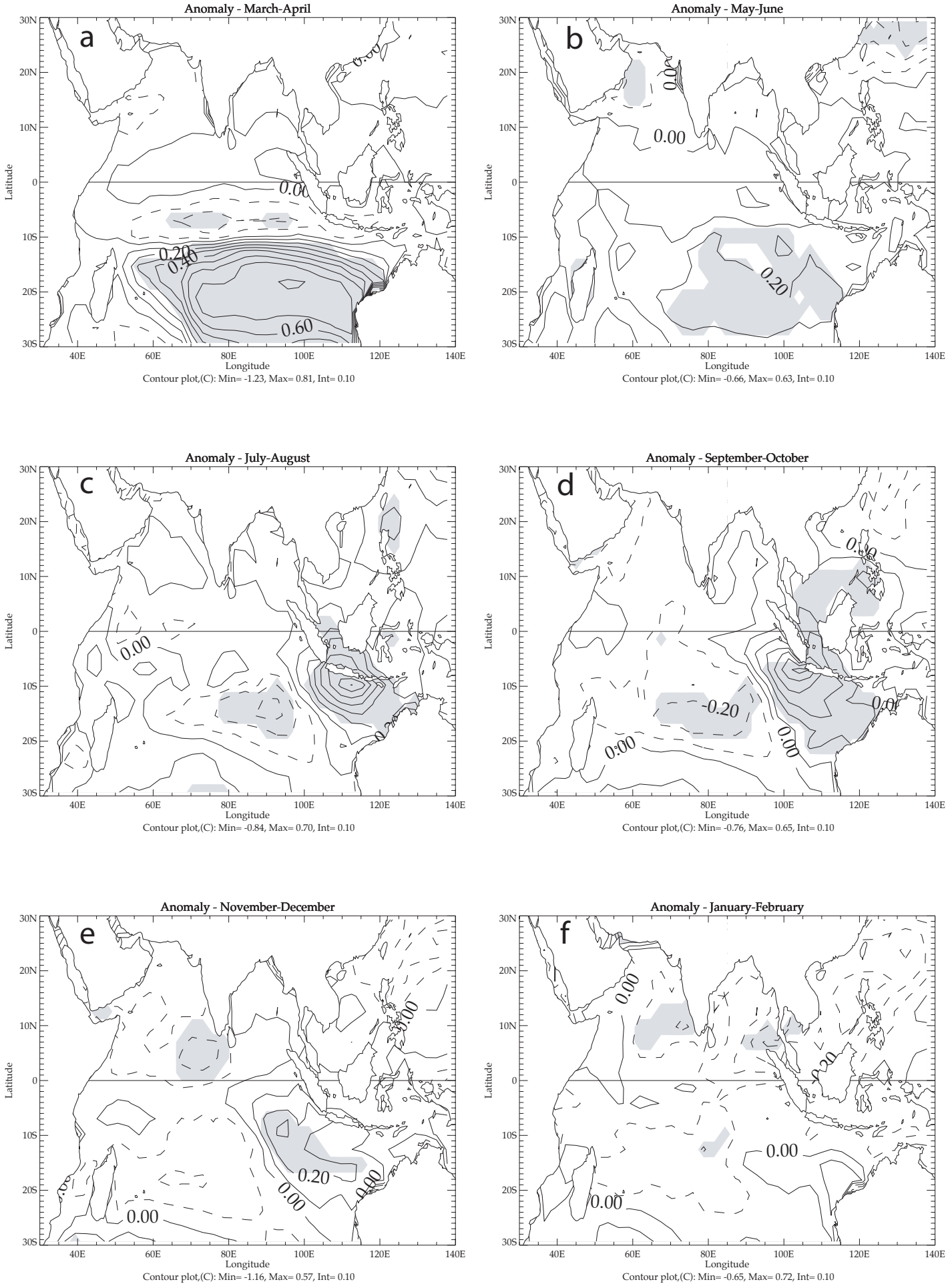

Figure 11

Positive - negative SEIO SST perturbations, 850 hPa wind and Rainfall, (No EL NINO years) year+1

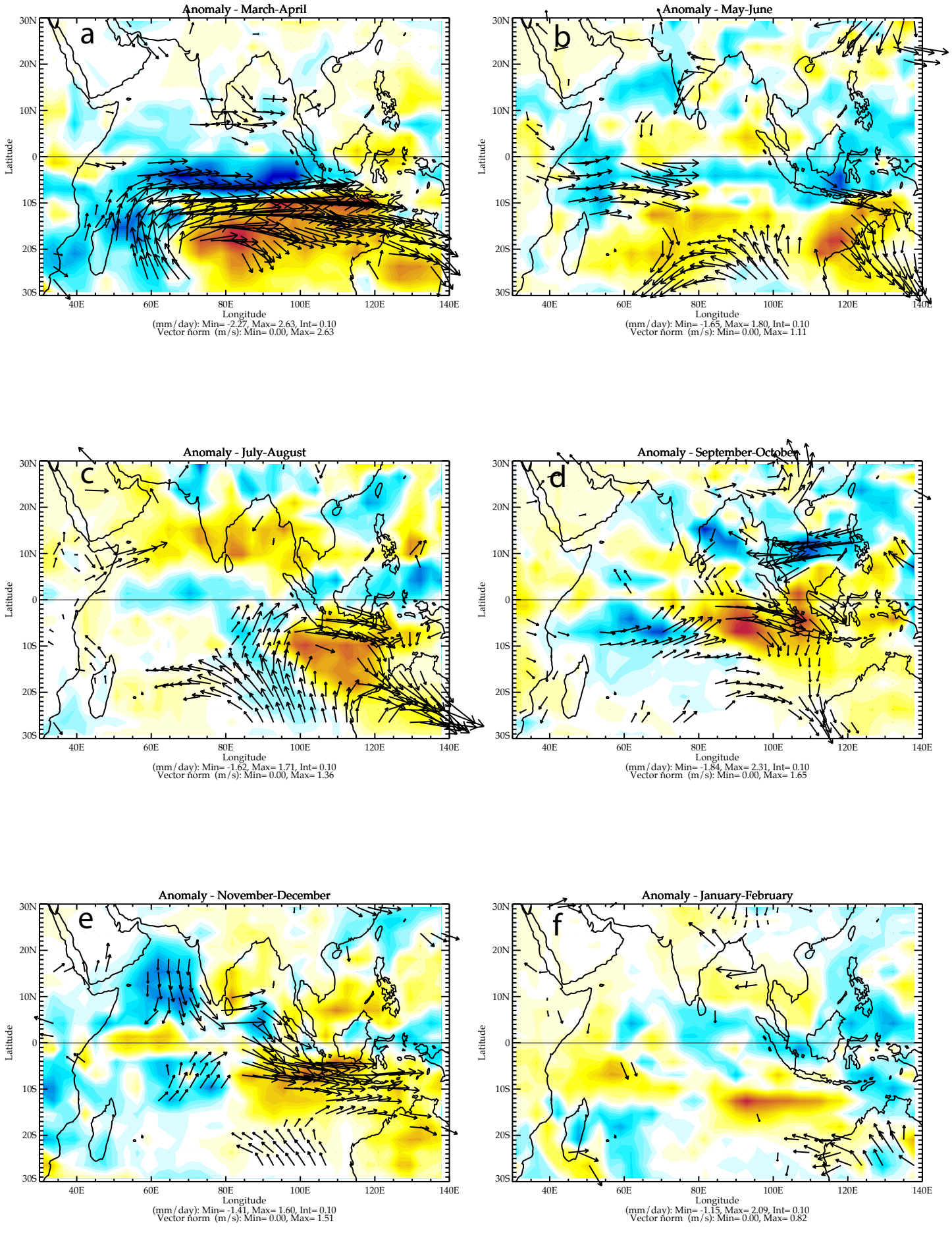

Figure 12

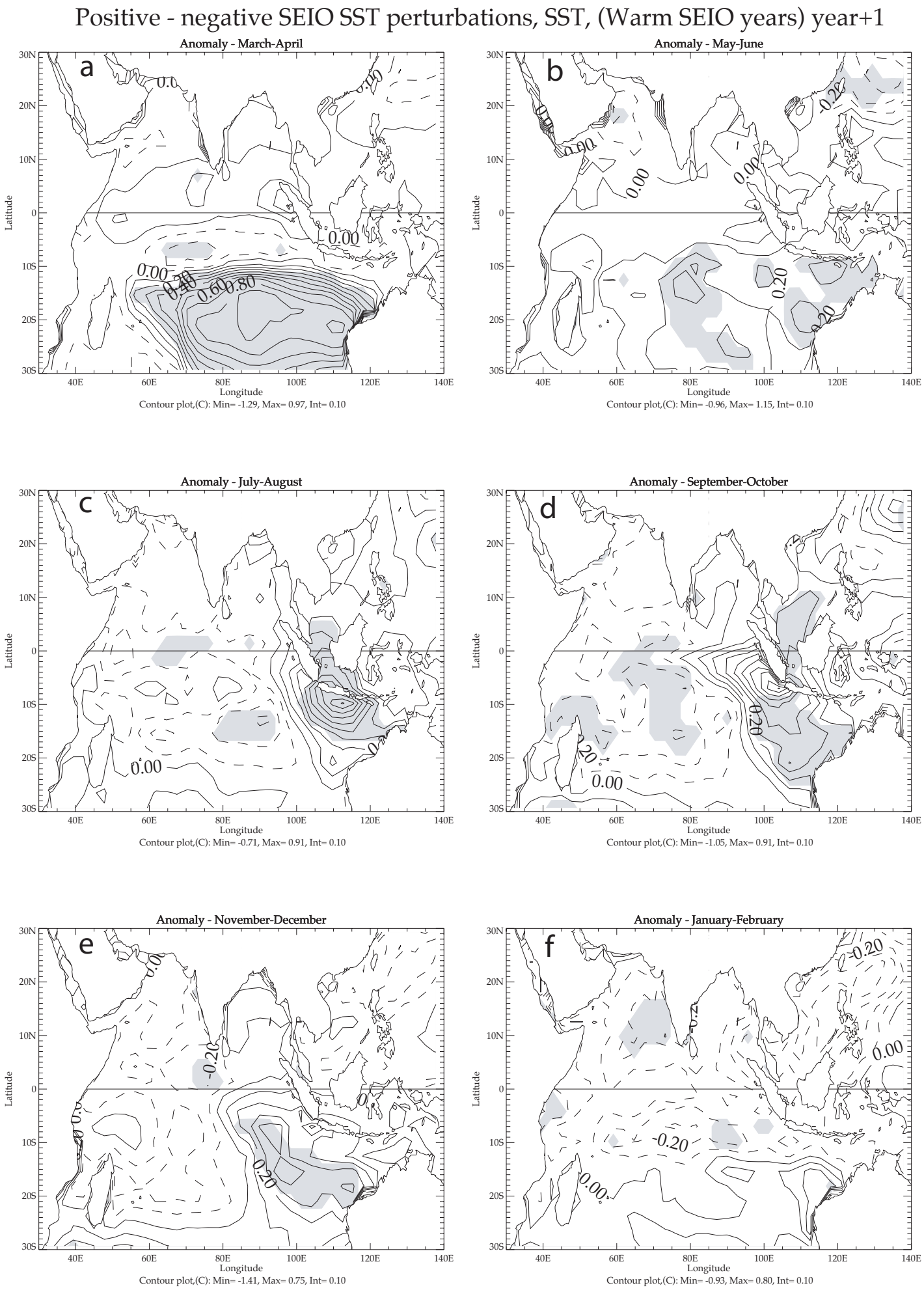
Positive - negative SEIO SST perturbations, SST, (Warm SEIO years) year+1
Anomaly - March-April
a
Contour plot,(C): Min= -1.29, Max= 0.97, Int= 0.10
Anomaly - May-June
b
Contour plot,(C): Min= -0.96, Max= 1.15, Int= 0.10
Anomaly - July-August
c
Contour plot,(C): Min= -0.71, Max= 0.91, Int= 0.10
Anomaly - September-October
d
Contour plot,(C): Min= -1.05, Max= 0.91, Int= 0.10
Anomaly - November-December
e
Contour plot,(C): Min= -1.41, Max= 0.75, Int= 0.10
Anomaly - January-February
f
Contour plot,(C): Min= -0.93, Max= 0.80, Int= 0.10
Latitude
Longitude
30N
20N
10N
0
10S
20S
30S
40E
60E
80E
100E
120E
140E

Figure 13

Positive - negative SEIO SST perturbations, 850 hPa wind and Rainfall, (Warm SEIO years) year+1

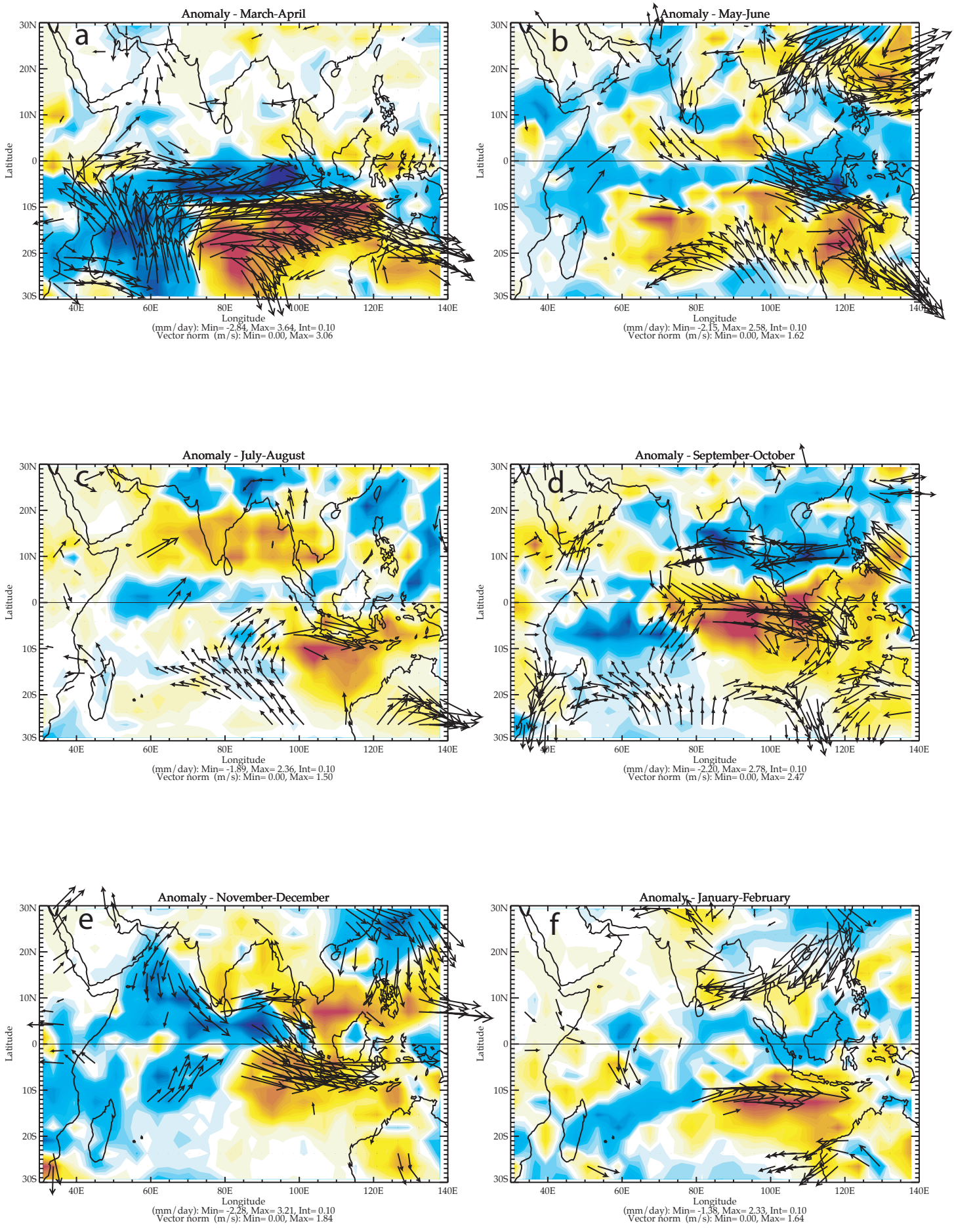

Figure 14

Positive - negative SEIO SST perturbations, Evaporation, (Warm SEIO years) year+1